J. Fluid Mech. (2000), *vol.* 421, *pp.* 39–81. Printed in the United Kingdom

Surface forced internal waves and vortices in uniformly stratified and rotating fluids

By RUDOLF C. KLOOSTERZIEL

School of Ocean and Earth Science and Technology, University of Hawaii, Honolulu,
HI 96822, USA

(Received 28 June 1999 and in revised form 15 May 2000)

The motion of an initially quiescent, incompressible, stratified and/or rotating fluid of semi-infinite extent due to surface forcing is considered. The stratification parameter N and the Coriolis parameter f are constant but arbitrary and all possible combinations are considered, including $N = 0$ (rotating homogeneous fluid), $f = 0$ (non-rotating stratified fluid) and the special case $N = f$. The forcing is suction or pumping at an upper rigid surface and the response consists of geostrophic flows and inertial-internal waves. The response to impulsive point forcings (Green's functions) is contrasted with the response to finite-sized circularly symmetric impulsive forcings. Early-time and large-time behaviour are studied in detail. At early times transient internal waves change the vortices that are created by pumping/suction at the surface. The asymptotically remaining vortices are determined, a simple expression for what fraction of the initial energy is converted into internal waves is derived, as well as wave energy fluxes and the dependence of the flux direction on the value of N/f. The internal wave field is to leading order in time a distinct pulse, and rules for the arrival time of the pulse, its amplitude, its motion along a ray of constant frequency and decay with time, are given for the far field. A simple formula for the total wave energy distribution as a function of frequency is derived for when all waves have propagated away from the forcing.

1. Introduction

We consider the response of a uniformly stratified and/or rotating fluid to surface forcing which is a prescribed vertical momentum flux w_s at an upper rigid surface. In a geophysical context this can be considered a study of the response of a continuously stratified ocean to wind-stress forcing at the surface. Charney (1955) showed that wind-stress forcing can be modelled by imposing a vertical velocity field which results from the divergence of a viscous Ekman layer generated by surface winds. If steady boundary layer dynamics is used (i.e. a balance between the Coriolis acceleration and the stress) then the Ekman pumping at the base of the Ekman layer is (Pedlosky 1979) $w_s = \boldsymbol{z} \cdot \nabla \wedge (\boldsymbol{\tau}/\rho_0 f)$, with f the Coriolis parameter, ρ_0 some average density, $\boldsymbol{\tau}$ the horizontal wind stress (vector), $\boldsymbol{z}$ the vertical unit vector pointing upwards and w_s the vertical Ekman pumping velocity (see figure 1). Such a flux excites an internal wave field and can generate geostrophically balanced vortices or currents. We assume the fluid layer to be initially quiescent and in its unperturbed state to have an exponential stratification so that the Brunt–Väisälä frequency N is constant. Fluid velocities are assumed small and the linearized dynamics for an inviscid and incompressible fluid are used. N and f are arbitrary and when $N \neq 0$ the Boussinesq

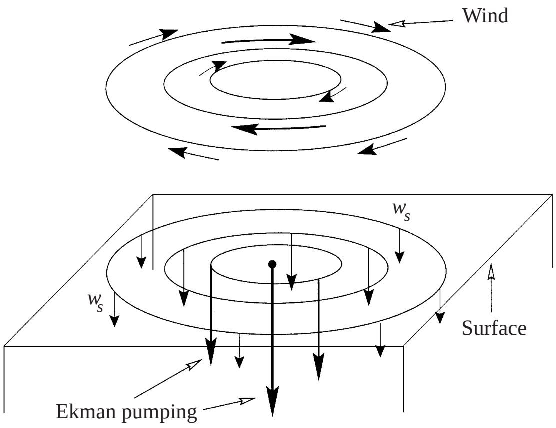

FIGURE 1. Diagram of how wind forcing leads to a vertical momentum flux w_s (see text). The surface in this diagram is the bottom of the surface Ekman layer. An anticyclone leads to pumping (as sketched), a cyclone to suction.

approximation is made, i.e. density variations are only taken into account when calculating buoyancy forces. We focus only on impulsive forcing, i.e. forcing of the form $w_s \propto \delta(t)$. Alternatively, this can be considered a study of how certain initial conditions evolve after the forcing has stopped. Some results for switch-on forcings will also be mentioned.

In § 2 we briefly review the equations that govern the dynamics under the above-mentioned approximations and the properties of linear inertial–internal waves that a rotating stratified fluid can support (e.g. Eckart 1960; Phillips 1963; Hendershott 1969; Lighthill 1978; Gill 1982). We continue with a derivation of the appropriate Green's function for the horizontal velocity components u and v, the vertical velocity w and pressure p. For given forcing w_s the response is $G_u \circ w_s$, $G_v \circ w_s$, $G_w \circ w_s$ and $G_p \circ w_s$, respectively, where $\circ$ indicates convolution of the surface data with the Green's function(s). The present study concerns only the semi-infinite domain. For a layer of constant depth with a rigid bottom and constant N, the (vector) Green's function can subsequently be constructed with the method of images but this is not done here.

In § 3 we study the early-time behaviour of the Green's functions, i.e. the velocity and pressure fields due to an impulsive point *sink* $w_s = \delta(x)\delta(y)\delta(t)$ (for a *source* signs need to be reversed). Cartesian coordinates $\{x, y, z\}$ are used, with $\{x, y\}$ the horizontal ones and z the vertical coordinate. We contrast the results with two cases of forcing of finite spatial scale. Both are circularly symmetric, i.e. functions of $r = (x^2 + y^2)^{1/2}$. One of them is $w_s = S(r;\varepsilon)\delta(t)$, where the parameter ε is a measure for the horizontal scale of the forcing. This function is such that $\lim_{\varepsilon\to 0} S(r;\varepsilon) \to \delta(x)\delta(y)$ and in this limit the singular behaviour of the Green's functions is recovered. The other, more complicated forcing is $w_s = -\partial_\varepsilon S(r;\varepsilon)\delta(t) = S'(r;\varepsilon)\delta(t)$. In § 3.1 early-time results are discussed for the Green's function when $N = f$ and in § 3.2 for the finite-sized forcings. This case is simple because the system cannot support propagating waves. It has a 'clay-like' property such that when the forcing stops a geostrophically balanced steady vortex immediately results. For $N \neq f$ there are after initial stages of potential flow and vortex formation additional adjustments which signal the start of internal wave radiation. Early-time expansions in § 3.3 and § 3.4 show that first a flow in the axial plane occurs. When $f \neq 0$ the Coriolis force acts on the horizontal component of the axial flow, which changes the vortex.

In § 4 the large-time behaviour of the response to an impulsive point sink or point source is investigated and contrasted with the finite-sized forcing $w_s = S(r;\varepsilon)\delta(t)$. For the other finite-sized forcing some results are presented but due to mathematical difficulties the analysis is far from complete. In § 4.1 we discuss the asymptotically remaining vortices and in § 4.2 the 'wavy' part of the response to point forcing. There are buoyancy oscillations when $N \neq 0$ (§ 4.2.1) which decay with time. Next (§ 4.2.2) we discuss the internal wave field and find that velocity amplitudes grow without bounds. Energy conservation appears violated but infinite energy is found to be stored in the initial condition which is the source of the wave energy. The wave energy flux is determined and we show how its direction varies as a function of N/f. In § 4.3 we calculate the energy stored in the initial conditions created by the two finite-sized forcings and the energy of the asymptotically remaining vortices. The difference is the energy available for the propagating internal waves and non-propagating oscillations. Section 4.4 concerns the asymptotic behaviour of the internal wave field and oscillations due to the finite-sized forcing. In § 4.4.1 we show that the internal waves propagate as a distinct pulse with amplitudes that remain finite at all times. Underneath the forcing there are regions where either no waves occur at large times or trapped waves with frequencies outside the range for freely propagating internal waves. For the far field an excellent analytical approximation is derived. We find simple formulas for when the pulse peaks as a function of observer position, the amplitude of the peak, how fast the pulse moves along a ray of constant frequency and how the amplitude of the peak decays as it moves along the ray. With the far-field approximation we also determine how energy is distributed over the internal wave frequency band. Finally, in § 4.4.2 the buoyancy oscillations are discussed and in § 4.4.3 the near-surface inertial oscillations which occur only for the finite-sized forcing.

In § 5 we summarize the main results and mention remaining unanswered questions as well as other matters of possible interest. Many mathematical details are in the Appendix.

2. Green's functions

With the assumptions and approximations mentioned in the introduction, the dynamics is governed by the equations

$$\frac{\partial \boldsymbol{u}}{\partial t} + \boldsymbol{f} \wedge \boldsymbol{u} + \frac{1}{\rho_0}\nabla p - b\boldsymbol{z} = 0, \quad \nabla \cdot \boldsymbol{u} = 0, \quad \frac{\partial b}{\partial t} + N^2 w = 0, \tag{1}$$

with $\boldsymbol{f} = f\boldsymbol{z}$, $\boldsymbol{u}$ the three-dimensional velocity vector, p pressure and b the buoyancy. The total density is given by $\rho = \bar{\rho}(z) + \rho'(x,y,z;t)$, where $\bar{\rho}(z)$ is an average background density, and $\rho'(x,y,z;t)$ the deviation from that mean. The pressure p is the deviation from the mean background pressure. In the Boussinesq approximation, $\bar{\rho}(z)$ has been replaced by an average value ρ_0 in the denominators of the pressure and buoyancy terms in (1), i.e. $b = -g\rho'/\rho_0$ with g the gravitational constant. N is the Brunt–Väisälä frequency: $N = [-(g/\bar{\rho})\partial_z\bar{\rho}]^{1/2}$ which is assumed constant (exponential stratification). By elimination the following equations for the vertical velocity w and pressure p (Gill 1982) and for the two horizontal velocity components, u and v, are found:

$$\left[\frac{\partial^2}{\partial t^2}\nabla^2 + f^2\frac{\partial^2}{\partial z^2} + N^2\nabla_{\mathrm{h}}^2\right]\{w,p\} = 0, \quad \partial_t^2\partial_z^2\left[\frac{\partial^2}{\partial t^2}\nabla^2 + f^2\frac{\partial^2}{\partial z^2} + N^2\nabla_{\mathrm{h}}^2\right]\{u,v\} = 0. \tag{2}$$

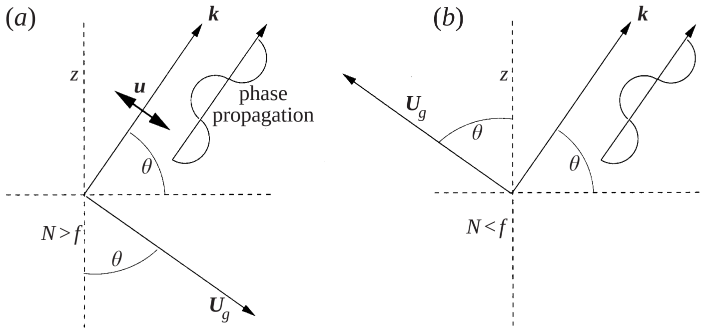

FIGURE 2. The relations between the direction of the wave vector $\boldsymbol{k}$, the group velocity $\boldsymbol{U}_{\mathrm{g}}$ and the direction of phase propagation of a plane wave in a rotating stratified fluid for (*a*) $N > f$ and (*b*) $N < f$. The velocity $\boldsymbol{u}$ is perpendicular to $\boldsymbol{k}$ and lies in the same plane as $\boldsymbol{U}_{\mathrm{g}}$.

∇^2 is the three-dimensional Laplace operator, ∇_{h}^2 the horizontal Laplace operator. The dispersion relation is obtained by putting a plane wave $\mathrm{e}^{\mathrm{i}(kx+ly+mz+\omega t)}$ in (2)

$$\omega^2 = f^2 \sin^2 \theta + N^2 \cos^2 \theta, \tag{3}$$

where θ is the angle between the wave vector $\boldsymbol{k} = (k, l, m)$ and the horizontal plane perpendicular to the axis of rotation, which is along the z-axis (see figure 2). If both f and N are non-zero, frequencies lie between f and N (we take f positive). The group velocity vector $\boldsymbol{U}_{\mathrm{g}}$ lies in the same plane as $\boldsymbol{k}$ but is perpendicular to it, i.e. $\boldsymbol{U}_{\mathrm{g}} \cdot \boldsymbol{k} = 0$. It has a magnitude

$$|\boldsymbol{U}_{\mathrm{g}}| = \frac{1}{|\boldsymbol{k}|} \frac{|N^2 - f^2|}{(N^2/\sin^2\theta + f^2/\cos^2\theta)^{1/2}} = \frac{|N^2 - \omega^2|^{1/2} |f^2 - \omega^2|^{1/2}}{|\boldsymbol{k}|\omega}. \tag{4}$$

Since $\boldsymbol{U}_{\mathrm{g}} \cdot \boldsymbol{k} = 0$, θ is also the angle between the group velocity vector and the *vertical* (see figure 2). The maximum group velocity for a given wave vector $\boldsymbol{k}$, the corresponding direction and frequency are

$$\boldsymbol{U}_{\mathrm{gmax}} = \frac{|N - f|}{|\boldsymbol{k}|}, \quad \cos^2 \theta_{\mathrm{max}} = \frac{f}{N + f}, \quad \omega_{\mathrm{max}}^2 = Nf. \tag{5}$$

The group velocity associated with either $\omega = f$ or $\omega = N$ is zero. When $N > f$, upward phase propagation implies downward group velocity and vice versa, whereas when $N < f$ phase propagation and group velocity are pointing both either up or down (see figure 2). In the limit $N = f$ a rotating stratified fluid cannot support propagating internal waves.

There are various ways to find the Green's functions. For our problem with a prescribed boundary condition at the surface, it is most convenient to derive $G_{\{u,v,w,p\}}$ as defined in the introduction directly from (1). In terms of components the set of equations (1) is

$$u_t - fv + p_x = 0, \quad v_t + fu + p_y = 0, \quad b_t + N^2 w = 0, \quad w_t + p_z - b = 0, \quad u_x + v_y + w_z = 0. \tag{6}$$

The boundary condition at $z = 0$ is

$$w(x, y, z = 0; t) = w_s(x, y; t). \tag{7}$$

We have non-dimensionalized the equations as follows: $t = Tt$, $\{x, y, z\} = L\{x, y, z\}$, $\{u, v, w\} = U\{u, v, w\}$, $p = (\rho_0 UL/T)p$, $b = (U/T)b$, $N^2 = N^2/T^2$ and $f = f/T$, where the left-hand sides are the original *dimensional* variables while the corresponding variables on the right are the non-dimensional ones appearing in (6). L and U are an arbitrary length scale and velocity scale, respectively. An arbitrary time scale T instead of f^{-1} or N^{-1} is used which makes it more convenient to investigate the limits $f = 0$ or $N = 0$. The forcing starts at $t = 0$ and initial conditions for the various fields need to be supplied. The following transforms are applied to (6): a Laplace transform in time, a Laplace transform in z, and a double Fourier transform in x, y. For convenience we use the variable $z' = -z$ so that underneath the surface z' is positive. The sequence of transforms is

$$\mathscr{L}_t = \int_0^{\infty} (\cdot)\mathrm{e}^{-\omega t}\,\mathrm{d}t \rightarrow \mathscr{L}_z = \int_0^{\infty} (\cdot)\mathrm{e}^{-sz'}\,\mathrm{d}z' \rightarrow \mathrm{FT} = \int_{-\infty}^{+\infty}\int_{-\infty}^{+\infty} (\cdot)\mathrm{e}^{\mathrm{i}kx+\mathrm{i}ly}\,\mathrm{d}x\,\mathrm{d}y. \tag{8}$$

After elimination of the buoyancy the following algebraic set of equations is found:

$$\begin{pmatrix} \omega & -f & 0 & -\mathrm{i}k \\ f & \omega & 0 & -\mathrm{i}l \\ 0 & 0 & (\omega^2 + N^2) & -s\omega \\ -\mathrm{i}k & -\mathrm{i}l & -s & 0 \end{pmatrix} \begin{pmatrix} u \\ v \\ w \\ p \end{pmatrix} = \begin{pmatrix} u_0 \\ v_0 \\ \omega w_0 + b_0 - \omega p_s \\ -w_s \end{pmatrix}, \tag{9}$$

where on the left-hand side $\{u, v, w, p\}(k, l, s; \omega)$ are the transforms of the corresponding fields and on the right-hand side $w_s(k, l; \omega)$ is the transform of the prescribed vertical velocity at the surface and $p_s(k, l; \omega)$ the transform of an as of yet undetermined surface pressure term. The quantities $\{u_0, v_0, w_0, p_0, b_0\}(k, l, s)$ are the transforms of the fields at $t = 0$, i.e. the initial conditions. In concise notation (9) is $\boldsymbol{A}\cdot\boldsymbol{x} = \boldsymbol{y}$, where $\boldsymbol{A}$ is the 4×4 matrix, $\boldsymbol{x} = (u, v, w, p)^{\mathrm{T}}$ and $\boldsymbol{y} = (u_0, v_0, (\omega w_0 + b_0 - \omega p_s), -w_s)^{\mathrm{T}}$ (T standing for transpose of the vectors). To solve for $\{u, v, w, p\}$ we need the inverse $\boldsymbol{A}^{-1}$ of $\boldsymbol{A}$ which is

$$\boldsymbol{A}^{-1} = \frac{1}{|\boldsymbol{A}|}\begin{pmatrix} -\omega^2 s^2 + l^2(\omega^2 + N^2) & -f\omega s^2 - kl(\omega^2 + N^2) & s(f\mathrm{i}l + \omega\mathrm{i}k) & (f\mathrm{i}l + \omega\mathrm{i}k)(\omega^2 + N^2) \\ f\omega s^2 - kl(\omega^2 + N^2) & -\omega^2 s^2 + k^2(\omega^2 + N^2) & s(\omega\mathrm{i}l - f\mathrm{i}k) & (\omega\mathrm{i}l - f\mathrm{i}k)(\omega^2 + N^2) \\ \omega s(\omega\mathrm{i}k - f\mathrm{i}l) & \omega s(\omega\mathrm{i}l + f\mathrm{i}k) & \omega(k^2 + l^2) & s\omega(\omega^2 + f^2) \\ (\omega\mathrm{i}k - f\mathrm{i}l)(\omega^2 + N^2) & (f\mathrm{i}k + \omega\mathrm{i}l)(\omega^2 + N^2) & s(\omega^2 + f^2) & (\omega^2 + f^2)(\omega^2 + N^2) \end{pmatrix}, \tag{10}$$

where $|\boldsymbol{A}| = \omega[(k^2 + l^2)(\omega^2 + N^2) - s^2(\omega^2 + f^2)]$. Assuming no initial motion and hydrostatic balance $(u_0, v_0, w_0, \mathrm{b}_0 = 0)$, it follows that

$$\left.\begin{aligned} u(k, l, s; \omega) &= (-f\mathrm{i}l - \omega\mathrm{i}k)[s\omega p_s + (\omega^2 + N^2)w_s]/|\boldsymbol{A}|, \\ v(k, l, s; \omega) &= (f\mathrm{i}k - \omega\mathrm{i}l)[s\omega p_s + (\omega^2 + N^2)w_s]/|\boldsymbol{A}|, \\ w(k, l, s; \omega) &= [-\omega^2(k^2 + l^2)p_s - s\omega(\omega^2 + f^2)w_s]/|\boldsymbol{A}|, \\ p(k, l, s; \omega) &= -(\omega^2 + f^2)[s\omega p_s + (\omega^2 + N^2)w_s]/|\boldsymbol{A}|. \end{aligned}\right\} \tag{11}$$

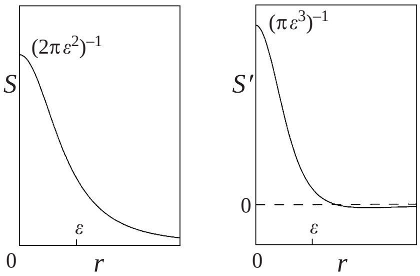

FIGURE 3. The functions (*a*) $S(r;\varepsilon)$ and (*b*) $S'(r,\varepsilon)$ defined by (16). Maximum amplitudes as a function of the parameter ε are as indicated.

Next we need to calculate the inverse transforms

$$\mathscr{L}_t^{-1} = \frac{1}{2\pi\mathrm{i}}\int_{-\mathrm{i}\infty}^{+\mathrm{i}\infty} (\cdot)\mathrm{e}^{\omega t}\,\mathrm{d}\omega, \quad \mathscr{L}_z^{-1} = \frac{1}{2\pi\mathrm{i}}\int_{-\mathrm{i}\infty}^{+\mathrm{i}\infty} (\cdot)\mathrm{e}^{sz'}\,\mathrm{d}s,$$

$$\mathrm{FT}^{-1} = \frac{1}{(2\pi)^2}\int_{-\infty}^{+\infty}\int_{-\infty}^{+\infty} (\cdot)\mathrm{e}^{-\mathrm{i}kx-\mathrm{i}ly}\,\mathrm{d}k\,\mathrm{d}l. \tag{12}$$

The contours for the inverse Laplace transforms run in the complex ω- and s-planes to the right of the singularities that occur in the expressions given by (11). In the Appendix the relation between the unknown surface pressure p_s and the prescribed surface forcing w_s is determined through an examination of the radiation condition. This accomplished, the transforms can be calculated and the result is

$$G_u = (f\partial_y + \partial_t\partial_x)\psi, \quad G_v = (-f\partial_x + \partial_t\partial_y)\psi,$$

$$G_w = \partial_z(\partial_t^2 + f^2)h, \quad G_p = -(\partial_t^2 + f^2)\psi, \tag{13}$$

with

$$\psi = \frac{U(t)}{2\pi R}\left\{ J_0(\omega_i t) + N\int_0^t\int_0^{t'} J_0(\omega_i(t'-t''))\frac{J_1(Nt'')}{t''}\,\mathrm{d}t''\,\mathrm{d}t' \right\},$$

$$h = \frac{U(t)}{2\pi R}\int_0^t J_0(\omega_i(t-t'))J_0(Nt')\,\mathrm{d}t', \tag{14}$$

and

$$\omega_i^2 = f^2(x^2+y^2)/R^2 + N^2z^2/R^2 = f^2\sin^2\theta + N^2\cos^2\theta, \quad R = (x^2+y^2+z^2)^{1/2}. \tag{15}$$

R is the distance from the origin and ω_i is the frequency of internal waves propagating from the source at an angle θ with the vertical to the observer location (see (3)). $U(t)$ is the Heaviside stepfunction and J_0, J_1 are Bessel functions. This is the response to $w_s(x,y;t) = \delta(x)\delta(y)\delta(t)$, i.e. an impulsive point sink. Changing signs everywhere gives the response to a source.

3. Green's functions and finite-sized forcings: early-time behaviour

The response to the point forcing $w_s = \delta(x)\delta(y)\delta(t)$ (Green's functions) is contrasted here and in subsequent sections with the response to two cases of circularly symmetric, finite-sized impulsive forcings $w_s = S(r;\varepsilon)\delta(t)$ and $w_s = S'(r;\varepsilon)\delta(t)$ defined by

$$S(r;\varepsilon) = \frac{\varepsilon}{2\pi(\varepsilon^2 + r^2)^{3/2}}, \quad S'(r;\varepsilon) = -\partial_\varepsilon S(r;\varepsilon) = \frac{2\varepsilon^2 - r^2}{2\pi(\varepsilon^2 + r^2)^{5/2}}. \tag{16}$$

Here $r = (x^2 + y^2)^{1/2}$ and $\varepsilon > 0$ is an arbitrary number. S and S' are shown in figure 3. The integrals $\int_{-\infty}^{+\infty}\int_{-\infty}^{+\infty} S(r;\varepsilon)\,\mathrm{d}x\,\mathrm{d}y = 1$ and $S \rightarrow \delta(x)\delta(y)$ in the limit $\varepsilon \rightarrow 0$. In this limit the results for $w_s = S(r;\varepsilon)\delta(t)$ must coincide with the results for the Green's function. For S there is suction for all r (figure 3*a*). Figure 3(*b*) shows that for S' there is a region near the centre where suction occurs, whereas further out pumping occurs. In this case $\int_{-\infty}^{+\infty}\int_{-\infty}^{+\infty} S'(r;\varepsilon)\,\mathrm{d}x\,\mathrm{d}y = 0$ and as much fluid as gets pumped in gets sucked out elsewhere.

3.1. *Special case $N = f$: Green's functions*

The limit $N = f$ leads to the simplest form of the Green's functions:

$$\psi = \frac{U(t)}{2\pi R}, \quad (\partial_t^2 + f^2)h = \frac{\delta(t)}{2\pi R}. \tag{17}$$

The horizontal velocity field is according to (13)

$$\boldsymbol{u}_\mathrm{h} = (G_u, G_v) = f\nabla_\mathrm{h} \wedge \boldsymbol{z}\psi + \nabla_\mathrm{h}\partial_t\psi, \tag{18}$$

where ∇_h is the horizontal gradient operator. With (13) we further find that

$$\boldsymbol{u} = \overbrace{\nabla\frac{\delta(t)}{2\pi R}}^{\boldsymbol{u}_\mathrm{p}} + \overbrace{f\nabla_\mathrm{h} \wedge \boldsymbol{z}\frac{U(t)}{2\pi R}}^{\boldsymbol{u}_\mathrm{vh}}, \quad p = \overbrace{-\frac{\delta'(t)}{2\pi R}}^{p_\mathrm{p}} + \overbrace{-f^2\frac{U(t)}{2\pi R}}^{p_\mathrm{v}}, \tag{19}$$

where a prime indicates a derivative. The first term of $\boldsymbol{u}$ represents potential flow $\boldsymbol{u}_\mathrm{p}$, the second term a vortex with a horizontal swirling flow $\boldsymbol{u}_\mathrm{vh}$. We use the additional subscript h to indicate horizontal components. In the initial stage of the response the dynamics proceeds as follows:

$$\overbrace{\partial_t\boldsymbol{u}_\mathrm{p} = -\nabla p_\mathrm{p}}^{(1)} \longrightarrow \overbrace{\partial_t\boldsymbol{u}_\mathrm{vh} = -f\boldsymbol{z} \wedge \boldsymbol{u}_\mathrm{ph}}^{(2)} \longrightarrow \overbrace{f\boldsymbol{z} \wedge \boldsymbol{u}_\mathrm{vh} = -\nabla_\mathrm{h} p_\mathrm{v}}^{(3)}, \tag{20}$$

that is, first potential flow is generated by the gradient of p_p, then the Coriolis force acts on the horizontal component of the potential flow $\boldsymbol{u}_\mathrm{p}$ to generate the swirling flow $\boldsymbol{u}_\mathrm{vh}$ which is in geostrophic balance with the pressure field p_v (see figure 4). Stage (1) shows that the Boussinesq fluid initially ignores both rotation and stratification in accordance with Batchelor's (1967) general discussion of the motion induced by impulsive motion of boundaries in a fluid (see also Morgan 1953).

In cylindrical polar coordinates (r, ϕ, z), velocity fields have components (u_r, u_ϕ, w) where u_r is the velocity in the radial direction, u_ϕ the velocity in the azimuthal direction and w is still the vertical velocity (see figure 5). The gradient is $\nabla = (\boldsymbol{e}_r\partial_r, \boldsymbol{e}_\phi r^{-1}\partial_\phi, \boldsymbol{z}\partial_z)$ with $\boldsymbol{e}_r$ the unit vector in the radial direction and $\boldsymbol{e}_\phi$ the unit vector in the azimuthal direction. The potential flow is

$$\boldsymbol{u}_\mathrm{p} = \delta(t)\left\{\frac{-r}{2\pi R^3}\boldsymbol{e}_r + \frac{-z}{2\pi R^3}\boldsymbol{z}\right\} = \frac{-\delta(t)}{2\pi R^3}\frac{\boldsymbol{R}}{R}, \quad R = (r^2 + z^2)^{1/2}, \tag{21}$$

where $\boldsymbol{R}$ is the position vector, and $\boldsymbol{R}/R$ the unit vector pointing from the sink position ($x = y = z = 0$) to the observer position (remember that underneath the surface z is negative). In figure 6(*a*) streamlines for (21) in the axial plane are superposed on the

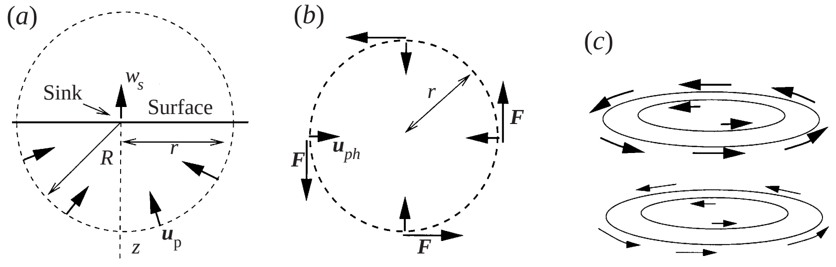

FIGURE 4. Initial stages of the response to a point sink $w_s = \delta(x)\delta(y)\delta(t)$ given by (20) (see text) with (*a*) side view of the potential flow $\boldsymbol{u}_\mathrm{p}$, (*b*) top view of the Coriolis acceleration $\boldsymbol{F} = -f\boldsymbol{z} \wedge \boldsymbol{u}_\mathrm{ph}$ and (*c*) perspective view of the resulting cyclone. Highest amplitudes occur near the surface.

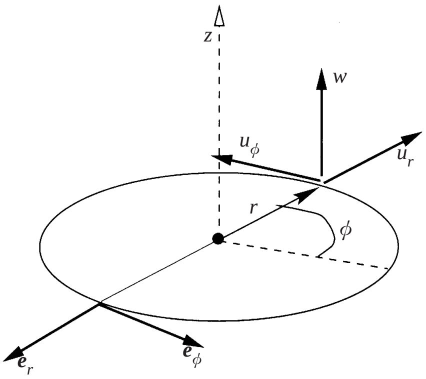

FIGURE 5. The cylindrical polar coordinate system (r, ϕ, z) and the corresponding velocity components (u_r, u_ϕ, w).

velocity amplitude. At the sink position $R = 0$, $\boldsymbol{u}_\mathrm{p}$ becomes infinite. The swirling flow is

$$\boldsymbol{u}_\mathrm{vh} = -f\partial_r\psi\boldsymbol{e}_\phi = fU(t)\frac{r}{2\pi(r^2+z^2)^{3/2}}\boldsymbol{e}_\phi. \tag{22}$$

It is in the direction of $\boldsymbol{e}_\phi$ everywhere, i.e. clockwise or cyclonic. The potential flow is towards the sink position and the creation of a cyclone is thus easily explained. By changing signs we get the response to a point source at the surface. The potential flow is then away from the source point and an anticyclone forms. In figure 7(*a*) $\boldsymbol{u}_\mathrm{vh}$ is shown at the surface and at some distance below the surface. At the surface $\boldsymbol{u}_\mathrm{vh}$ becomes infinite at the sink position $r = 0$.

FIGURE 7. Velocity amplitudes (colour) of the cyclones $\boldsymbol{u}_\mathrm{vh}$ for (*a*) $w_s = \delta(x)\delta(y)\delta(t)$ given by (22), (*b*) $w_s = S(r;\varepsilon)\delta(t)$ given by (25) and (*c*) $w_s = S'(r;\varepsilon)\delta(t)$ given by (27). In (*a*) velocity amplitudes have been deleted between $z = -\varepsilon$ and the surface $z = 0$. Amplitudes have been normalized by the maximum in each case. Above, the velocity profiles at the surface $z = 0$ and $z = -\varepsilon$ are shown. For the point sink (*a*) the velocity approaches infinity near $z = r = 0$. The velocity profiles in (*b*) and (*c*) have been normalized by the maximum that occurs at the surface. In (*a*) they have been normalized with the maximum that occurs at $z = -\varepsilon$. For a description of the difference between the cyclones shown in (*b*) and (*c*) see text. The profile in (*a*) at $z = -\varepsilon$ is equal to that in (*b*) at $z = 0$.

FIGURE 8. Contours (white) of the Stokes streamfunction ψ_s for the $O(t)$-axial flow for (*a*) $w_s = \delta(x)\delta(y)\delta(t)$ given by (30), (*b*) $w_s = S(r;\varepsilon)\delta(t)$ given by (32) and (*c*) $w_s = S'(r;\varepsilon)\delta(t)$ given by (33). Colouring indicates velocity amplitudes normalized by the maximum. In (*a*) velocities have been deleted in an area around the sink where they get very large. The dotted line in (*a*) and (*b*) marks the dividing line between the zones of inward and outward acceleration. Flow directions depend on the value of N/f (see text).

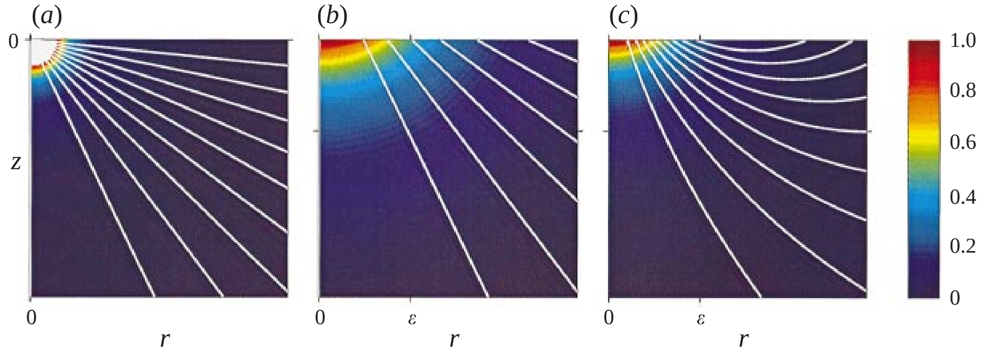

FIGURE 6. Streamlines (white) plus velocity amplitudes (colour) for the potential flow $\boldsymbol{u}_\mathrm{p}$ for (*a*) $w_s = \delta(x)\delta(y)\delta(t)$ given by (21), (*b*) $w_s = S(r;\varepsilon)\delta(t)$ given by (24) and (*c*) $w_s = S'(r;\varepsilon)\delta(t)$ given by (26). In (*a*) velocity amplitudes have been deleted in a small hemisphere surrounding the point sink where they tend to infinity. Amplitudes have been normalized by the maximum; the flow is inwards along the streamlines; for sources the flows are outwards.

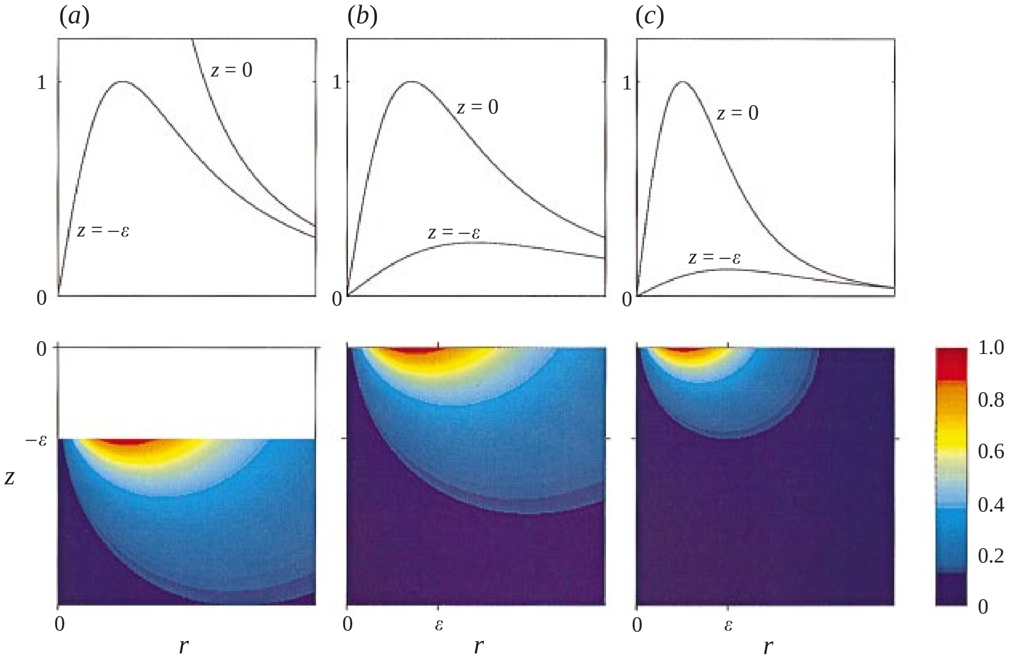

FIGURE 7. For caption see facing page.

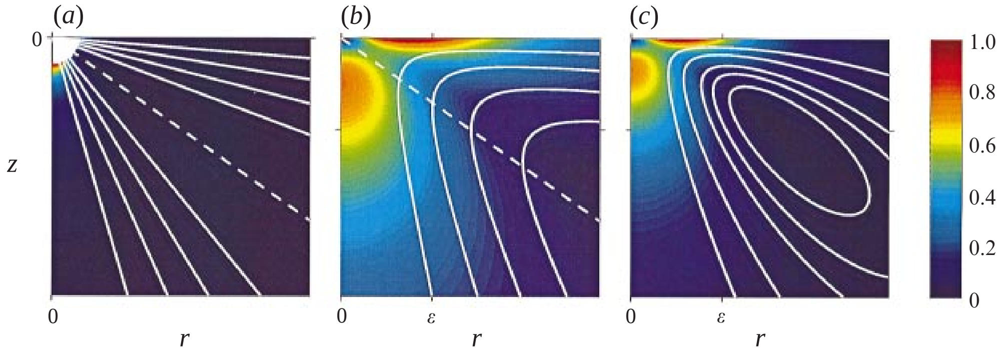

FIGURE 8. For caption see facing page.

For forcing $w_s = \delta(x)\delta(y)F(t)$ with $F(t)$ some rate of pumping/suction the solution is

$$\boldsymbol{u} = \nabla\frac{F(t)}{2\pi R} + f\nabla_{\rm h}\wedge \boldsymbol{z}\frac{M(t)}{2\pi R}, \quad p = -\frac{F'(t)}{2\pi R} - f^2\frac{M(t)}{2\pi R}, \tag{23}$$

where $M(t) = \int_0^t F(t')\mathrm{d}t'$. The amplitude of the vortex is proportional to the removed or injected mass $M(t)$. Irrespective of the time-dependence of the forcing, the potential flow and the vortex become unbounded as one approaches the source position $R = 0$. The singular behaviour disappears when finite-sized forcings are used.

3.2. *Special case $N = f$: finite-sized forcings*

Now consider the example of the circularly symmetric forcing $w_s = S(r;\varepsilon)\delta(t)$ with S defined in (16) and shown in figure 3(*a*). The potential flow is

$$\boldsymbol{u}_{\rm p} = \delta(t)\left\{\frac{-r}{2\pi R_\varepsilon^3}\boldsymbol{e}_r + \frac{(-z+\varepsilon)}{2\pi R_\varepsilon^3}\boldsymbol{z}\right\} = \frac{-\delta(t)}{2\pi R_\varepsilon^3}\frac{\boldsymbol{R}_\varepsilon}{R_\varepsilon}, \quad R_\varepsilon = (r^2 + (-z+\varepsilon)^2)^{1/2}. \tag{24}$$

$\boldsymbol{R}_\varepsilon$ is the position vector measured from an apparent δ-sink position *above* the surface at $z = \varepsilon$. Streamlines for (24) in the axial plane and the velocity amplitude are shown in figure 6(*b*). At the surface $z = 0$ the vertical component of $\boldsymbol{u}_{\rm p}$ is equal to $w_s = S(r;\varepsilon)\delta(t)$, i.e. the boundary condition is satisfied and $\boldsymbol{u}_{\rm p}$ is well-behaved for all r and $z \leqslant 0$. The vortex is a cyclone

$$\boldsymbol{u}_{\rm vh} = fU(t)\frac{r}{2\pi(r^2 + (-z+\varepsilon)^2)^{3/2}}\boldsymbol{e}_\phi, \tag{25}$$

which is also well-behaved for all r and $z \leqslant 0$ as is seen in figure 7(*b*) where $\boldsymbol{u}_{\rm vh}$ is shown at the surface and at some distance below it. In the limit $\varepsilon \to 0$ (21) and (22) are recovered. For $w_s = -S(r;\varepsilon)$ (pumping instead of suction) the sign in (25) changes, and an anticyclone forms. For switch-on forcing $w_s = S(r;\varepsilon)F(t)$, (23) holds with R replaced by R_ε, that is, $\delta(t)$ in (24) is replaced by $F(t)$ and $U(t)$ in (25) by $M(t)$.

The response to the forcing $w_s = S'(r;\varepsilon)\delta(t)$, with S' defined in (16) and shown in figure 3(*b*), is obtained by taking the $-\partial_\varepsilon$-derivative of (24) and (25):

$$\boldsymbol{u}_{\rm p} = \delta(t)\left\{\frac{-3r(-z+\varepsilon)}{2\pi R_\varepsilon^5}\boldsymbol{e}_r + \frac{2(-z+\varepsilon)^2 - r^2}{2\pi R_\varepsilon^5}\boldsymbol{z}\right\} \tag{26}$$

and

$$\boldsymbol{u}_{\rm vh} = fU(t)\frac{3r(-z+\varepsilon)}{2\pi(r^2 + (-z+\varepsilon)^2)^{5/2}}\boldsymbol{e}_\phi. \tag{27}$$

Streamlines for (26) in the axial plane and the velocity amplitude are shown in figure 6(*c*). Although the net mass flux is zero a cyclone forms whereas for $w_s = -S'\delta(t)$ an anticyclone results. In the latter case there is pumping near the centre and suction at larger r (figure 3*b* with the sign of S' changed). Figure 7(*c*) shows $\boldsymbol{u}_{\rm vh}$, at the surface and below it. This cyclone decays faster with depth than the one shown in figure 7(*b*) when there was suction everywhere. The latter has its maximum at $r = (-z+\varepsilon)/\sqrt{2}$ and the amplitude there is proportional to $(-z+\varepsilon)^{-2}$ whereas the vortex of figure 7(*c*) has its maximum at $r = (-z+\varepsilon)/2$ with an amplitude proportional to $(-z+\varepsilon)^{-3}$. There is also a difference in the horizontal in that the vortex of figure 7(*b*) decays with r^{-2} for large r whereas the vortex of figure 7(*c*) decays with r^{-4}.

3.3. *General case $N \neq f$: Green's functions*

The above completes the analysis for $N = f$ for all times. No matter what forcing is used, geostrophically balanced flows result. In the general case however there are subsequent adjustments. The response to $w_s = \delta(x)\delta(y)\delta(t)$ at early times is

$$\psi = \frac{U(t)}{2\pi R} + U(t)\frac{(N^2 - f^2)r^2}{8\pi R^3}t^2 + O(t^4),$$

$$(\partial_t^2 + f^2)h = \frac{\delta(t)}{2\pi R} + U(t)\frac{(f^2 - N^2)(r^2 + 2z^2)}{4\pi R^3}t + O(t^3). \tag{28}$$

The first terms are as before, the second terms represent adjustments that follow when $N \neq f$. There is an $O(t)$-flow in the axial plane with radial and vertical velocity

$$u_r = U(t)\frac{(N^2 - f^2)r(2z^2 - r^2)}{4\pi(r^2 + z^2)^{5/2}}t, \quad w = -U(t)\frac{(N^2 - f^2)z(r^2 - 2z^2)}{4\pi(r^2 + z^2)^{5/2}}t. \tag{29}$$

The two velocity components are related to a Stokes streamfunction ψ_s according to

$$u_r = -\frac{1}{r}\frac{\partial \psi_s}{\partial z}, \quad w = \frac{1}{r}\frac{\partial \psi_s}{\partial r}, \quad \psi_s = U(t)\frac{(N^2 - f^2)zr^2}{4\pi(r^2 + z^2)^{3/2}}t. \tag{30}$$

Contours of ψ_s and the velocity amplitude are shown in figure 8(*a*). The velocity vector in the (r, z)-plane is along lines of constant ψ_s, defined by $z/r =$ constant. According to (29) for $N > f$ there is at early times a tendency for the fluid to accelerate radially inward in the near-surface region $|z| < r/\sqrt{2}$ and radially outward where $|z| > r/\sqrt{2}$. The dotted line is the dividing line $|z| = r/\sqrt{2}$ between the inflow and outflow regions. For $N < f$ directions are reversed: outflow near the surface and inflow at greater depths. The inflow and outflow meet at the sink position where amplitudes become infinite. Integration over the surface of an arbitrarily small hemisphere placed around the sink position shows that the net mass flux associated with the $O(t)$ potential flow is zero. Consequently, an equal amount of fluid moving towards the singular point (sink position) flows out elsewhere. The singular behaviour near the sink position obscures how the inflow and outflow are connected. The inward flow near the surface ($N > f$ case) is acted upon by the Coriolis force when $f \neq 0$, and stronger cyclonic flow near the surface results. The outward flow at greater depths similarly leads to a decrease in cyclonic flow. For weak stratification ($N < f$) directions are reversed and opposite tendencies result, i.e. less cyclonic motion near the surface and more at greater depths. This is clear from the $O(t^2)$ correction to (22)

$$\boldsymbol{u}_{\text{vh}} = fU(t)\frac{r}{2\pi(r^2 + z^2)^{3/2}}\left[1 + (N^2 - f^2)\frac{r^2 - 2z^2}{4(r^2 + z^2)}t^2 + O(t^4)\right]\boldsymbol{e}_\phi. \tag{31}$$

For an impulsive point source, directions are reversed: an anticyclone is created when $f \neq 0$ while at $O(t)$ for $N > f$ there is an outward flow near the surface and an inward flow where $|z| > r/\sqrt{2}$. For $N > f$ the anticyclone increases in strength near the surface, for $N < f$ it weakens.

3.4. *General case $N \neq f$: finite-sized forcings*

For the finite-sized forcing $w_s = S(r; \varepsilon)\delta(t)$ there is again first potential flow (24) and then vortex formation (25) (when $f \neq 0$) as in the special case $N = f$. This is followed by an $O(t)$-flow in the axial plane with streamfunction

$$\psi_s = U(t)\frac{(N^2-f^2)zr^2}{4\pi(r^2+(-z+\varepsilon)^2)^{3/2}}t. \tag{32}$$

Contours of ψ_s and the velocity amplitude are shown in figure 8(*b*). When the sink was infinitely concentrated at the surface ($\varepsilon = 0$), for $N > f$ a radial inflow near the surface occurred, while there was an outflow away from the sink position in the lower region (figure 8*a*). Both inflow and outflow appeared to collide at the singular point $r = z = 0$. With this sink of finite size, we see how the inwards accelerating flow is connected to the outflow. Figure 8(*b*) shows that the fluid which accelerates up and towards the axis $r = 0$ turns around and then accelerates away from the axis. In the limit $\varepsilon \to 0$ the pattern of figure 8(*a*) is recovered. For $N < f$ flow directions reverse.

For the forcing $w_s = S'(r;\varepsilon)\delta(t)$ the quickest way to obtain the response is by taking the $-\partial_\varepsilon$-derivative of the expressions for $w_s = S(r;\varepsilon)\delta(t)$. For $N \neq f$ (26) and (27) are again the initial potential flow and vortex, respectively. For the $O(t)$-flow

$$\psi_s = -\partial_\varepsilon(32) = U(t)\frac{3(N^2-f^2)z(-z+\varepsilon)r^2}{4\pi(r^2+(-z+\varepsilon)^2)^{5/2}}t. \tag{33}$$

Contours of ψ_s plus the velocity amplitude are shown in figure 8(*c*). A markedly different pattern is seen here as compared to the streamlines for the $O(t)$-flow shown in figure 8(*b*). No matter how far we ‘zoom out’ in the latter, flow lines never connect. In the present case the streamlines are closed. But, when $N > f$ the flow near the surface is again inwards and at greater depths outwards. When $N < f$ these directions are reversed. In both cases the Coriolis force accelerates the $O(t)$ axial flow in the azimuthal direction. This results in an $O(t^2)$-change to the vortex (25)

$$\boldsymbol{u}_{\mathrm{vh}} = fU(t)\frac{r}{2\pi(r^2+(-z+\varepsilon)^2)^{3/2}}\left[1+(N^2-f^2)\frac{r^2-2z^2+\varepsilon z+\varepsilon^2}{4(r^2+(-z+\varepsilon)^2)}t^2+O(t^4)\right]\boldsymbol{e}_\phi. \tag{34}$$

In the limit $\varepsilon \to 0$ this is (31). For $N > f$ the $O(t)$-inflow near the surface (small $|z|$) leads to stronger cyclonic flow near the surface while the outflow at greater depths (large $|z|$) leads to a decrease in cyclonic flow. For weak stratification ($N < f$) opposite tendencies result, i.e. less cyclonic motion near the surface and more at greater depths. The $O(t^2)$ correction to (27) i.e. $-\partial_\varepsilon(34)$, looks less simple than (34) but the same tendencies result. The $O(t)$-flows (30), (32) and (33) signal the onset of internal wave propagation. The Coriolis force acts on the internal wave motion which modifies the vortices. The waves propagate away and the vortices ultimately reach an equilibrium, which is discussed below.

4. Green’s functions and finite-sized forcings: large-time behaviour

4.1. *Vortices*

For the impulsive forcings discussed above the horizontal velocity, pressure and vertical velocity are $\boldsymbol{u}_{\mathrm{h}} = f\nabla_{\mathrm{h}} \wedge z\psi + \nabla_{\mathrm{h}}\partial_t\psi$, $p = -(\partial_t^2 + f^2)\psi$ and $w = \partial_z(\partial_t^2 + f^2)h$. Simple asymptotic techniques discussed in the Appendix show that for large times the response can generally be broken up in several distinct pieces: $\psi = \psi_\infty + \psi_N + \psi_f + \psi_i$ and $h = h_N + h_f + h_i$ where the subscripts N, f and i indicate buoyancy oscillations, inertial oscillations and internal waves, respectively, and the subscript ∞ an asymptotically steady, non-oscillatory component. When $f \neq 0$ a vortex remains in the limit $t \to \infty$ with a streamfunction ψ_∞ and swirling velocity $\boldsymbol{u}_{\mathrm{vh}\infty} = -f\partial_r \psi_\infty \boldsymbol{e}_\phi$:

$$w_s = \delta(x)\delta(y)\delta(t): \quad \psi_\infty = \frac{N/f}{2\pi(r^2+(N/f)^2z^2)^{1/2}},$$

$$\boldsymbol{u}_{\mathrm{vh}\infty} = \frac{Nr}{2\pi(r^2+(N/f)^2z^2)^{3/2}}\boldsymbol{e}_\phi, \tag{35}$$

$$w_s = S(r;\varepsilon)\delta(t): \quad \psi_\infty = \frac{N/f}{2\pi(r^2+(-(N/f)z+\varepsilon)^2)^{1/2}},$$

$$\boldsymbol{u}_{\mathrm{vh}\infty} = \frac{Nr}{2\pi(r^2+(-(N/f)z+\varepsilon)^2)^{3/2}}\boldsymbol{e}_\phi, \tag{36}$$

$$w_s = S'(r;\varepsilon)\delta(t): \quad \psi_\infty = -\partial_\varepsilon \frac{N/f}{2\pi(r^2+(-(N/f)z+\varepsilon)^2)^{1/2}},$$

$$\boldsymbol{u}_{\mathrm{vh}\infty} = \frac{3Nr(-(N/f)z+\varepsilon)}{2\pi(r^2+(-(N/f)z+\varepsilon)^2)^{5/2}}\boldsymbol{e}_\phi. \tag{37}$$

Comparing these expressions with (22), (25) and (27) we find that at the surface ($z=0$) the swirling velocity distribution is as before but has changed in amplitude by a factor N/f. Instead of z we have $(N/f)z$ everywhere which implies that for $N>f$ the vortices are asymptotically more confined in the vertical with higher amplitudes than initially and for $N<f$ more stretched in the vertical with lower amplitudes, as anticipated in § 3.3 and § 3.4. For decreasing N the vortices get more spread out in the vertical, which can be interpreted as a tendency towards Taylor-column formation, with a decreasing overall amplitude. In the limit $N=0$ (rotating homogeneous fluid) the vortices asymptotically vanish. In §3.1 and § 3.2 we showed that when $N=f$ no propagating waves exist and that when in each case $\delta(t)$ is replaced by some $F(t)$ (switch-on forcing) the vortex's amplitude is at any instant proportional to $M(t)=\int_0^t F(t')\,\mathrm{d}t'$. It is not when $N \neq f$ but under some mild restrictions on $F(t)$ (see Appendix) that asymptotically the vortex's amplitude will be proportional to $M(\infty)$.

4.2. *Asymptotic waves and buoyancy oscillations for Green's functions*

For the Green's function there are asymptotically internal waves and when $N \neq 0$ buoyancy oscillations:

$$\left.\begin{aligned}
\psi_N &= 2\mathrm{Re}\,\frac{N\mathrm{e}^{\mathrm{i}(Nt+\pi/4)}}{(2\pi)^{3/2}R(N^2-\omega_i^2)^{1/2}}\frac{1}{(Nt)^{3/2}}[1+\Upsilon_{\psi_N}],\\
h_N &= 2\mathrm{Re}\,\frac{\mathrm{e}^{\mathrm{i}(Nt-3\pi/4)}}{(2\pi)^{3/2}R(N^2-\omega_i^2)^{1/2}}\frac{1}{(Nt)^{1/2}}[1+\Upsilon_{h_N}],\\
\psi_i &= 2\mathrm{Re}\,\frac{(N^2-\omega_i^2)^{1/2}\mathrm{e}^{\mathrm{i}(\omega_i t-3\pi/4)}}{(2\pi)^{3/2}R\omega_i}\frac{1}{(\omega_i t)^{1/2}}[1+\Upsilon_{\psi_i}],\\
h_i &= 2\mathrm{Re}\,\frac{\mathrm{e}^{\mathrm{i}(\omega_i t-\pi/4)}}{(2\pi)^{3/2}R(N^2-\omega_i^2)^{1/2}}\frac{1}{(\omega_i t)^{1/2}}[1+\Upsilon_{h_i}].
\end{aligned}\right\} \tag{38}$$

Here Re stands for the real part of the complex expressions. When $N = 0$ there are only propagating internal waves and $\psi_N = h_N = 0$. The asymptotic errors are

$$\Upsilon_{\psi_N}, \Upsilon_{h_N} = O((Nt)^{-1}, t_N^{-1}), \quad \Upsilon_{\psi_i}, \Upsilon_{h_i} = O((\omega_i t)^{-1}, t_i^{-1}),$$
$$t_N = |N^2 - \omega_i^2| t/N, \quad t_i = |N^2 - \omega_i^2| t/\omega_i. \tag{39}$$

For $N = 0$ the leading-order behaviour of ψ_i, h_i is valid to a high degree of precision when $(\omega_i t)^{-1} \ll 1$. Since $\omega_i = f|\sin\theta|$ when $N = 0$ (θ is defined in figure 2), it follows that in the region of low-frequency oscillations $\omega_i \ll f$ (a vertical cone about the axis $r = 0$ with $|\sin\theta|$ small) the algebraic decay of the oscillations occurs later than in the high-frequency region $\omega_i \approx f$ near the surface. In the general case the leading-order behaviour of the buoyancy and internal wave components is valid when the scaled times $\{(Nt), t_N\} \gg 1$, $\{(\omega_i t), t_i\} \gg 1$, respectively. Thus again in the vertical cone with $|\sin\theta|$ small where $\omega_i \approx N$ the algebraic decay of the oscillations occurs later than near the surface where $\omega_i \approx f$. When $f = 0$ there is an additional region near the surface (with $\theta \approx \pi/2$) where the required waiting period is long because there $\omega_i \approx 0$.

4.2.1. *Buoyancy oscillations*

The velocity components of the buoyancy oscillations are

$$\{u_r, u_\phi, w\} = 2\mathrm{Re}\, \frac{\{Nr, \mathrm{i}fr, Nz\} N \mathrm{e}^{\mathrm{i}(Nt - \pi/4)}}{(2\pi)^{3/2} r^3 (N^2 - f^2)^{1/2}} \frac{1}{(Nt)^{3/2}} [1 + O((Nt)^{-1}) + O(t_N^{-1})]. \tag{40}$$

If $Nt \gg 1$ the leading-order behaviour is only correct when also $t_N \gg 1$, i.e. for large $|z|$ where $\omega_i \to N$ the behaviour given by the first term occurs later than near the surface (small $|z|$) where $\omega_i \approx f$; w and u_r are in phase and in the limit $f = 0$, $u_\phi = 0$ and there are just radial oscillations along lines θ = constant as noted by Voisin (1991) in a slightly different problem (internal point source/sink in an unbounded stratified fluid). Our solution when $f = 0$ is a modification of that case in that a u_ϕ-component is generated by the Coriolis force acting on the horizontal component of the radial pulsations ($\partial_t u_\phi = -f u_r$). At the surface the motion is horizontal with a velocity vector which rotates in clockwise direction when $f \neq 0$ with an elliptical polarization. The ratio of the axes in the azimuthal direction and the radial direction of the ellipse is f/N. With increasing time the horizontal velocity amplitude becomes depth-independent in areas where $t_N \gg 1$. This is outside a cone about the vertical axis with an angle θ that decreases with time. At the sink position ($r, z = 0$) amplitudes remain infinite at all times.

4.2.2. *Internal gravity waves*

For the internal gravity wave components of the Green's function we need to differentiate ψ_i and h_i. Since ω_i is a function of the spatial coordinates, differentiation brings down terms $\mathrm{i}\partial_r\omega_i t, \mathrm{i}\partial_z\omega_i t$ from the exponent and to leading order the amplitudes of the internal gravity wave components *grow* with $t^{1/2}$:

$$\{u_r, u_\phi, w\} \approx 2\mathrm{Re}\, \frac{\{\omega_i r, \mathrm{i}fr, \omega_i z\}(f^2 - \omega_i^2)(N^2 - \omega_i^2)^{1/2} \mathrm{e}^{\mathrm{i}(\omega_i t + \pi/4)}}{(2\pi)^{3/2} R^3 \omega_i^3} (\omega_i t)^{1/2}$$
$$\equiv \{u_r^{1/2}, u_\phi^{1/2}, w^{1/2}\}. \tag{41}$$

Superscripts 1/2 indicate components that grow with $t^{1/2}$. For $f = 0$ this reduces to results (apart from a factor 2) cited by Voisin (1991) for the internal wave field due

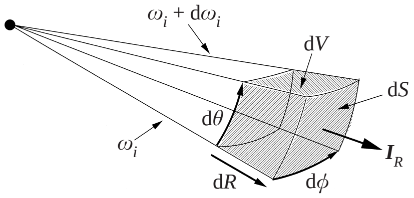

FIGURE 9. Diagram showing a volume element $\mathrm{d}V = R^2 \sin\theta\,\mathrm{d}\phi\,\mathrm{d}\theta\,\mathrm{d}R$ and an area element $\mathrm{d}S = R^2 \sin\theta\,\mathrm{d}\phi\,\mathrm{d}\theta$ on a sphere of constant R. ω_i is constant on rays of θ = constant (see figure 2). The rate of change of wave energy W is determined by the net radial energy flux $\boldsymbol{I}_R$ into the volume element dV.

to a point source in an unbounded stratified fluid. Unbounded growth of the total energy density $W = \frac{1}{2}(u_r^2 + u_\phi^2 + w^2) + \frac{1}{2}N^2\xi^2$ occurs, with $\xi = \int w\,\mathrm{d}t$ the vertical displacement. This appears to violate energy conservation but this is not so. The reason is that the unbalanced initial condition contains infinite energy. For instance when we integrate over the half-space $z < 0$ in spherical coordinates, we find that the initial vortex (22) has total kinetic energy

$$E_k(0) = \int_0^\infty \int_0^{\pi/2} \int_0^{2\pi} \tfrac{1}{2}|\boldsymbol{u}_{\mathrm{vh}}|^2 R^2 \sin\theta\,\mathrm{d}\phi\,\mathrm{d}\theta\,\mathrm{d}R = \frac{f^2}{4\pi}\int_0^\infty \int_0^{\pi/2} \frac{\sin^3\theta}{R^2}\,\mathrm{d}\theta\,\mathrm{d}R,$$

which is infinite. The initial displacement $\xi = \int^{0^+} w_{\mathrm{p}}\,\mathrm{d}t$, with w_{p} the vertical velocity of the potential flow (21), is $\xi = -z/2\pi R^3$. The initial total potential energy is

$$E_p(0) = \tfrac{1}{2}N^2 \int_0^\infty \int_0^{\pi/2} \int_0^{2\pi} \xi^2 R^2 \sin\theta\,\mathrm{d}\phi\,\mathrm{d}\theta\,\mathrm{d}R = \frac{N^2}{4\pi}\int_0^\infty \int_0^{\pi/2} \frac{\cos^2\theta\sin\theta}{R^2}\,\mathrm{d}\theta\,\mathrm{d}R,$$

which is also infinite. An unlimited supply of energy is therefore stored in the initial condition.

The time rate of change of the energy density is $\partial_t W = -\nabla\cdot\boldsymbol{I}$ with the wave energy flux $\boldsymbol{I} = p\boldsymbol{u}$ (Lighthill 1978). To leading order

$$p = -(\partial_t^2 + f^2)\psi_i \approx 2\mathrm{Re}\,\frac{(f^2 - \omega_i^2)(N^2 - \omega_i^2)^{1/2}\mathrm{e}^{\mathrm{i}(\omega_i t + \pi/4)}}{(2\pi)^{3/2} R\omega_i(\omega_i t)^{1/2}} \equiv p^{-1/2}, \tag{42}$$

which *decays* with $t^{-1/2}$. Combining the components of $\boldsymbol{I} = p^{-1/2}[u_r^{1/2}\boldsymbol{e}_r + u_\phi^{1/2}\boldsymbol{e}_\phi + w^{1/2}\boldsymbol{z}]$ along $\boldsymbol{e}_r$ and $\boldsymbol{z}$ into a radial component in spherical coordinates

$$\boldsymbol{I} = \cos^2(\omega_i t + \phi_i)\frac{4(f^2 - \omega_i^2)^2|N^2 - \omega_i^2|}{(2\pi)^3 R^3 \omega_i^3}\frac{\boldsymbol{R}}{R} + I_\phi \boldsymbol{e}_\phi, \quad I_\phi = p^{-1/2}u_\phi^{1/2}. \tag{43}$$

The phase $\phi_i = \pi/4$ when $N > f$ and $3\pi/4$ when $N < f$. If this is averaged over a period $\Delta t = 2\pi/\omega_i$ we get $\overline{I}_\phi = 0$ (a bar indicating the time-average) because $p^{-1/2}$ and $u_\phi^{1/2}$ are 90° out of phase. But, $p^{-1/2}$ and $u^{1/2}, w^{1/2}$ are in phase. On average the wave flux is thus along the vector $\boldsymbol{R}/R$, i.e. along lines of θ = constant or constant ω_i. For $\nabla\cdot\boldsymbol{I}$ the second term in (43) is irrelevant anyway because the fields do not depend on the angle ϕ. Defining $W' = WR^2\sin\theta$ so that W' is the energy density for volume elements dV spanned by $\mathrm{d}\phi\,\mathrm{d}\theta\,\mathrm{d}R$ (see figure 9), we find

$$\partial_t W' = [1 + \cos 2\varphi(t)]F(\omega_i, R), \quad F = \frac{2(f^2 - \omega_i^2)^2|N^2 - \omega_i^2|^{3/2}}{(2\pi)^3|N^2 - f^2|^{1/2}\omega_i^3}\frac{1}{R^2}, \tag{44}$$

with $\varphi(t)$ the argument of the cosine in (43). Time-integration shows that on average

W' increases linearly with time, obviously because of the $t^{1/2}$-growth of the velocity components.

Since we have exact expressions for the leading-order behaviour we can directly calculate W'. The kinetic energy density associated with the radial oscillations is

$$E_{kR}^{1/2} = \tfrac{1}{2}[(u_r^{1/2})^2 + (w^{1/2})^2]R^2 \sin\theta = t[1 + \cos 2\varphi(t)]F/2. \tag{45}$$

The kinetic energy density of the azimuthal velocity component is

$$E_{k\phi}^{1/2} = \tfrac{1}{2}(u_\phi^{1/2})^2 R^2 \sin\theta = t[1 - \cos 2\varphi(t)]\left(\frac{f^2 r^2}{\omega_i^2 R^2}\right)F/2. \tag{46}$$

The displacement $\xi = \int_0^t w\,\mathrm{d}t'$ is

$$\xi \approx 2\mathrm{Re}\,\frac{\{-\mathrm{i}z\}(f^2 - \omega_i^2)(N^2 - \omega_i^2)^{1/2}\mathrm{e}^{\mathrm{i}(\omega_i t + \pi/4)}}{(2\pi)^{3/2}R^3\omega_i^3}(\omega_i t)^{1/2} \equiv \xi^{1/2}; \tag{47}$$

$\xi^{1/2}$ is 180° out of phase with $u_\phi^{1/2}$. The potential energy density is

$$E_p^{1/2} = \tfrac{1}{2}N^2(\xi^{1/2})^2 R^2 \sin\theta = t[1 - \cos 2\varphi(t)]\left(\frac{N^2 z^2}{\omega_i^2 R^2}\right)F/2. \tag{48}$$

$E_{k\phi}^{1/2}$ and $E_p^{1/2}$ are zero when $E_{kR}^{1/2}$ is maximal and vice versa. It follows that

$$W' = E_{kR}^{1/2} + E_{k\phi}^{1/2} + E_p^{1/2} = tF. \tag{49}$$

It is not clear why Lighthill's flux recipe (44) does give the correct result when averaged over time but appears not correct for any t, not even for a stratified fluid ($f = 0$) for which he derived the theory.

By solving $\partial_{\omega_i}F = 0$, it is found that at any time for $f = 0$ (non-rotating stratified fluid) the wave energy density W' has a maximum at the angle $\theta_{\max} = \pi/3$, in the limit $f \to N$ at $\theta_{\max} = \pi/4$ and for $N = 0$ (rotating homogeneous fluid) at $\theta_{\max} = 0$. We have plotted $R^2 \times W'$ in figure 10 for a few combinations of f and N. At a given time this only depends on θ and clearly shows how W' varies with θ.

If we consider a small volume element $\mathrm{d}V$ as sketched in figure 9, then the rate of change of wave energy is determined by the difference between the flux that leaves the volume at $R + \mathrm{d}R$ and what enters at R. On average it is only the radial component $\boldsymbol{I}_R$ of $\boldsymbol{I}$ (the first component in (43)) that pumps energy into the volume element. The radial flux through a small area element $\mathrm{d}S$ on a sphere $R =$ constant (see figure 9) is $\boldsymbol{I}_R R^2 \sin\theta\,\mathrm{d}\phi\,\mathrm{d}\theta = \boldsymbol{I}'_R\,\mathrm{d}\phi\,\mathrm{d}\theta$, where $\boldsymbol{I}'_R$ is the radial flux for given R per unit area measured by θ and ϕ. It has a magnitude

$$|\boldsymbol{I}'_R| = [1 + \cos 2\varphi(t)]FR. \tag{50}$$

Thus, the radial flux varies with θ just as the wave energy density (49) does. At any instant the quantity $|\boldsymbol{I}'_R| \times R$ like $W' \times R^2$ depends only on θ and figure 10 therefore also provides a picture of how the flux varies with direction. It shows that the flux rotates away from the horizontal towards the vertical as N becomes smaller. For $N = 0$ the maximum flux is in the vertical ($\theta_{\max} = 0$), when $f = 0$ the maximum flux is at the angle $\theta_{\max} = \pi/3$. Comparison of (50) and (45) shows that $|\boldsymbol{I}'_R|$ and $E_{kR}^{1/2}$ vary in the same fashion with θ. Thus, not surprisingly, the highest flux occurs where the radial oscillations have the highest amplitudes.

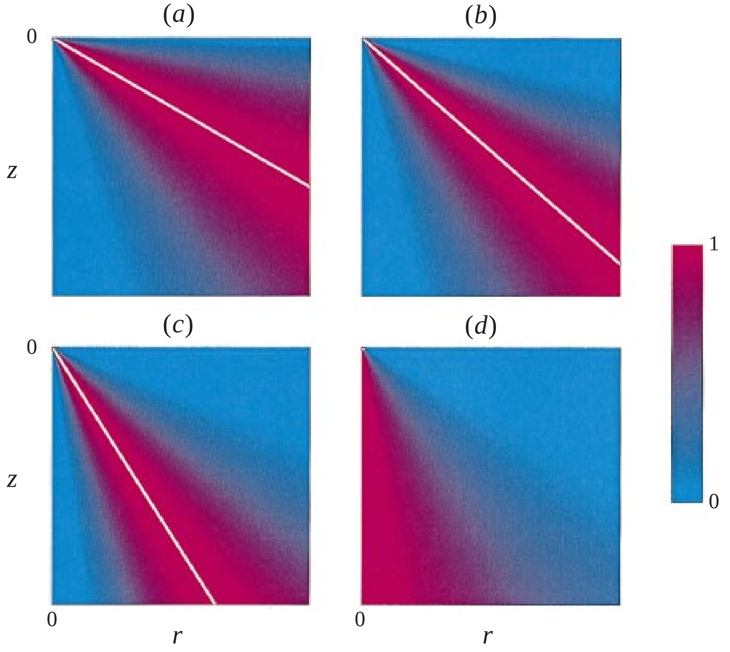

FIGURE 10.

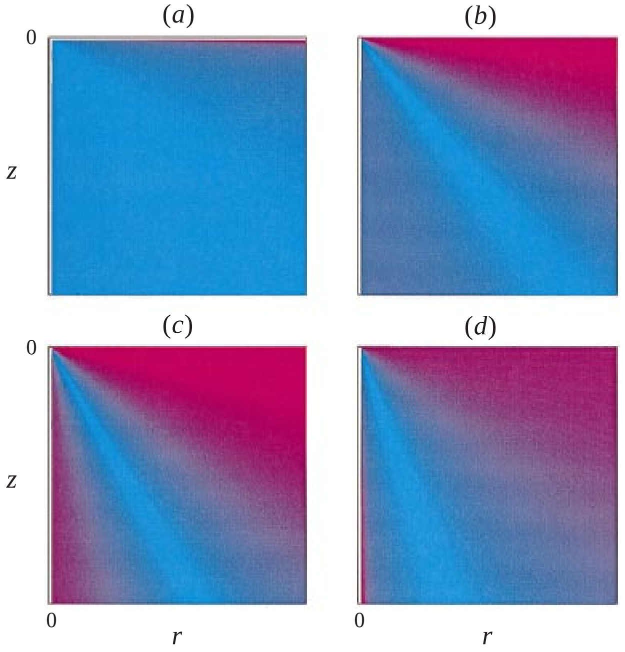

FIGURE 11.

FIGURE 10. The wave energy density W' given by (49) at a given time multiplied by R^2 and normalized by the maximum for (*a*) $f = 0$, (*b*) $N = 2f$, (*c*) $f = 2N$ and (*d*) $N = 0$. Also, the magnitude of the radial flux $|\boldsymbol{I}'_R|$ given by (50) at a given time multiplied by R (see text). White lines show rays at an angle $\theta_{\max}$ with the vertical along which the flux/energy is maximal. $\theta_{\max} = \pi/3$ when $f = 0$, $\theta_{\max} = 0.27\pi$ for $N = 2f$, $\theta_{\max} = 0.18\pi$ for $f = 2N$ and $\theta_{\max} = 0$ when $N = 0$.

FIGURE 11. The kinetic energy density $E_{kR}^{-1/2} \times R^2$ associated with the $O(t^{-1/2})$-radial oscillations and normalized by the maximum for (*a*) $f = 0$, (*b*) $N = 2f$, (*c*) $f = 2N$ and (*d*) $N = 0$. They can also be interpreted as showing the total wave energy density (multiplied by R^2) associated with the $t^{-1/2}$-velocity components and vertical displacement of the internal wave field. For $N = 0$ the radial oscillations vanish at $\sin\theta = 1/3$, for $f = 0$ at $\sin\theta = 2/3$.

The $O(t^{-1/2})$-correction for the gravity waves is

$$\{u_r^{-1/2}, u_\phi^{-1/2}, w^{-1/2}\} = 2\,\mathrm{Re}\,\frac{\{\omega_i r U(\omega_i), \mathrm{i} f r V(\omega_i), \omega_i z U(\omega_i)\}(N^2-\omega_i^2)^{1/2}\mathrm{e}^{\mathrm{i}(\omega_i t+3\pi/4)}}{(2\pi)^{3/2}R^3\omega_i(\omega_i t)^{1/2}}, \tag{51}$$

where

$$U(\omega_i) = 1 + \tfrac{1}{2}(f^2-\omega_i^2)[(N^2-\omega_i^2)^{-1} + (3/4)\omega_i^{-2}], \quad V(\omega_i) = U(\omega_i) + \tfrac{1}{2}(f^2-\omega_i^2)\omega_i^{-2}.$$

When $f \neq 0$ there are inertial oscillations at the surface:

$$\{u_r^{-1/2}, u_\phi^{-1/2}\}_{z=0} = 2\mathrm{Re}\,\frac{\{f, \mathrm{i}f\}(N^2-f^2)^{1/2}\,\mathrm{e}^{\mathrm{i}(ft+3\pi/4)}}{(2\pi)^{3/2}r^2(ft)^{1/2}}.$$

The $t^{-1/2}$-component (51) complements the $O(t^{1/2})$-component (41) in that where the latter has small amplitudes in space (disregarding the time-dependence) the former has not. To illustrate this we show in figure 11 $R^2 \times E_k^{-1/2}$ with $E_{kR}^{-1/2}$ defined like $E_{kR}^{1/2}$. This is for some fixed time: $E_k^{-1/2}$ decays with t^{-1} whereas $E_k^{1/2}$ grows with t. The angular areas of low amplitude seen in figure 11 are centred about an angle $\theta_{\min}$ where $u^{-1/2}$ and $w^{-1/2}$ vanish, i.e. where $U(\omega_i) = 0$. As one crosses $\theta_{\min}$ the phase of the radial oscillations jumps by a factor π (on both sides of $\theta_{\min}$ the oscillations are 180° out of phase). Note that $|u_r^{1/2}/u_\phi^{1/2}| = \omega_i/f$, $u_r^{1/2}/w^{1/2} = r/z = -\tan\theta$, i.e. the polarization relations for freely propagating internal waves in a rotating fluid are satisfied (Gill 1982). This is not true for the $t^{-1/2}$-components in (51) because $U(\omega_i) \neq V(\omega_i)$.

4.3. *Loss of initial energy to internal waves and oscillations*

In each case of the impulsive forcing discussed an initial condition is set up which evolves into propagating waves, non-propagating decaying oscillations and when $f, N \neq 0$, an asymptotically steady vortex. For convenience we refer to both the internal waves and the oscillations as 'waves'. We determine here how much of the initial total energy $E_{\mathrm{tot}}(0) = E_k(0) + E_p(0)$ (kinetic plus potential) goes to them. For the Green's function $E_{\mathrm{tot}}(0)$ is infinite and the internal wave amplitudes could accordingly grow without bounds. For the finite-sized forcings $E_{\mathrm{tot}}(0)$ is finite. We have to calculate $E_{\mathrm{tot}}(0)$ for both cases and also the kinetic energy of the asymptotic vortex $E_k^{\mathrm{v}}(\infty)$ and the potential energy associated with the asymptotically remaining vertical displacement field $E_p^{\mathrm{v}}(\infty)$. The superscript v indicates that these quantities are associated with the vortex. The energy E_i that has gone into the waves is then

$$E_i = E_{\mathrm{tot}}(0) - [E_k^{\mathrm{v}}(\infty) + E_p^{\mathrm{v}}(\infty)]. \tag{52}$$

$E_k(0) = \int |\boldsymbol{u}_{\mathrm{vh}}|^2\,\mathrm{d}V$ where $\int \mathrm{d}V$ indicates integration over the half-space $z \leqslant 0$ and $\boldsymbol{u}_{\mathrm{vh}}$ is from either (25) or (27). The initial vertical displacement $\xi = \int^{0^+} w_{\mathrm{p}}\,\mathrm{d}t$ equals the vertical velocity component w_{p} of the potential flow (24) or (26), and $E_p(0) = \frac{1}{2}N^2 \int \xi^2\,\mathrm{d}V$. Further, $E_k^{\mathrm{v}}(\infty) = \int |\boldsymbol{u}_{\mathrm{vh}\infty}|^2\,\mathrm{d}V$ where $\boldsymbol{u}_{\mathrm{vh}\infty}$ is (36) or (37). For $E_p^{v}(\infty) = \frac{1}{2}N^2 \int \xi^2(\infty)\,\mathrm{d}V$ we have to determine $\xi(\infty) = \int_0^\infty w\,\mathrm{d}t$. The result is

$$w_s = S(r;\varepsilon)\delta(t): \quad \xi(\infty) = \frac{(-(N/f)z+\varepsilon)}{2\pi(r^2+(-(N/f)z+\varepsilon)^2)^{3/2}},$$

$$w_s = S'(r;\varepsilon)\delta(t): \quad \xi(\infty) = \frac{2(-(N/f)z+\varepsilon)^2 - r^2}{2\pi(r^2+(-(N/f)z+\varepsilon)^2)^{5/2}}.$$

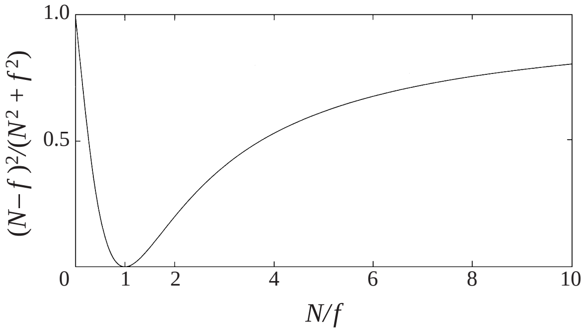

FIGURE 12. Fraction of total initial energy $E_{\mathrm{tot}}(0)$ converted to internal waves and oscillations for both finite-sized forcings $w_s = S(r;\varepsilon)\delta(t)$ and $w_s = S'(r;\varepsilon)\delta(t)$.

To calculate the energy of the initial conditions we employ a coordinate system with the origin at $z = \varepsilon$ and use spherical coordinates $\{R_\varepsilon, \theta, \phi\}$ with R_ε defined by (24). For the asymptotic energy calculations we use the same coordinate system but with z replaced by $(N/f)z$ in R_ε. With constants σ and ς for $w_s = S(r;\varepsilon)\delta(t)$ and σ' and ς' for $w_s = S'(r;\varepsilon)\delta(t)$ we find

$$E_k(0) = \{\sigma, \sigma'\}f^2, \quad E_p(0) = \{\varsigma, \varsigma'\}N^2, \quad E_k^v(\infty) = \{\sigma, \sigma'\}Nf, \quad E_p^v(\infty) = \{\varsigma, \varsigma'\}Nf. \tag{53}$$

Despite the fact that the integrals are quite different, $\sigma = \varsigma = (1/4)(4\pi\varepsilon)^{-1}$ and $\sigma' = \varsigma' = (9/24)(12\pi\varepsilon^3)^{-1}$. In both cases

$$\frac{E_k^v(\infty) + E_p^v(\infty)}{E_{\mathrm{tot}}(0)} = \frac{E_{\mathrm{tot}}^v(\infty)}{E_{\mathrm{tot}}(0)} = \frac{2Nf}{N^2 + f^2}.$$

For all combinations of $N \neq f$ the ratio is smaller than one. When $f = 0$ or $N = 0$ this vanishes because then there is no asymptotic vortex and all energy stored in the initial condition goes to the waves. In the limit $N = f$ the right-hand side equals one, which is when the system cannot support propagating waves and the initial vortex remains unchanged. The energy E_i (52) that goes to the waves is

$$E_i = \frac{(N-f)^2}{N^2 + f^2} E_{\mathrm{tot}}(0). \tag{54}$$

In figure 12 we show how $E_i/E_{\mathrm{tot}}(0)$ varies with N/f. Taking $f \neq 0$ it shows that for $N = 0$ the initial vortex in the semi-infinitely deep rotating homogeneous fluid disappears and all energy goes to the waves. When $N = f$ no waves are excited and for large N/f most energy goes again to the waves.

4.4. *Asymptotic waves and oscillations for a finite-sized forcing*

We investigate the asymptotic properties here of the oscillatory part of the response to the forcing $w_s = S(r;\varepsilon)\delta(t)$. It requires a careful examination of the properties of the inverse Laplace transform $\mathscr{L}_t^{-1}$ of a complicated function. In order not to distract from the main results, mathematical details are in the Appendix. In the complex ω-plane this function has a pole at $\omega = 0$ which determines the asymptotic vortices discussed above. There are branch points at $\omega = \pm\mathrm{i}N$ giving rise to buoyancy oscillations, branch points at $\omega = \pm\mathrm{i}f$ which give inertial oscillations and four movable branch points, two of which are 'visible' on the Riemann sheet where the inverse transform takes place. They are (where $\star$ stands for complex conjugate)

$$\omega_- = -\omega_r + \mathrm{i}\omega_i^\varepsilon, \quad \omega_-^\star = -\omega_r - \mathrm{i}\omega_i^\varepsilon, \tag{55}$$

where

$$\omega_-^2 = \frac{\varrho^2 N^2 - f^2}{1-\varrho^2}, \quad \varrho = z/(\mathrm{i}r - \varepsilon). \tag{56}$$

They determine the internal wave field of which the velocity components have amplitudes that vary to leading order with $t^{1/2}\,\mathrm{e}^{-\omega_r t + \mathrm{i}\omega_i^\varepsilon t}$, disregarding complex phase factors and spatial dependence of amplitudes. Contours of the distribution of ω_i^ε are shown in figure 13. In each example there are regions underneath the surface, bounded in the horizontal by $r = \varepsilon$, where ω_i^ε is outside the frequency range of propagating internal waves. No contours have been drawn there of ω_i^ε: they are closed and if waves exist there, they are trapped. All frequencies meet at the singular point $z = -\varepsilon$. Contours of ω_r are shown in figure 14. In each case ω_r is large near the singular point $z = -\varepsilon$. Regions where ω_r exceeds the highest possible frequency that can occur in the system have been left empty. In areas of large ω_r the waves will rapidly disappear. In the Appendix we derive the approximations

$$\omega_i^{\varepsilon 2} \approx \omega_i'^2 = \frac{f^2(r^2+\varepsilon^2)}{R'^2} + \frac{N^2 z^2}{R'^2}, \quad \omega_r \approx \frac{-\varepsilon z|(f^2-\omega_i'^2)^{1/2}(N^2-\omega_i'^2)^{1/2}|}{\omega_i' R'^2},$$

$$R' = (r^2+z^2+\varepsilon^2)^{1/2}. \tag{57}$$

Figures 13 and 14 show that these are good approximations far from the forcing region. For $r, |z| \gg \varepsilon$ both ω_i^ε and its far-field approximation ω_i' become constant on cones of constant angle θ, i.e. they approach ω_i defined by (15).

4.4.1. *Internal gravity waves*

To leading order the velocity components of the internal wave field are

$$\{u_r^{1/2}, u_\phi^{1/2}, w^{1/2}\}$$
$$= 2\mathrm{Re}\,\frac{\{\omega_i^\varepsilon r, (\mathrm{i}\omega_i^\varepsilon/\omega_-)\mathrm{i}fr, \omega_i^\varepsilon(z+\varepsilon\varrho)\}(f^2+\omega_-^2)(N^2+\omega_-^2)^{1/2}\mathrm{e}^{-\omega_r t + \mathrm{i}(\omega_i^\varepsilon t + \pi/4)}}{(2\pi)^{3/2}R'^3 P^{3/2}\omega_i^{\varepsilon 3}}(\omega_i^\varepsilon t)^{1/2}, \tag{58}$$

the pressure is

$$p^{-1/2} = 2\mathrm{Re}\,\frac{(\mathrm{i}\omega_i^\varepsilon/\omega_-)(f^2+\omega_-^2)(N^2+\omega_-^2)^{1/2}\mathrm{e}^{-\omega_r t + \mathrm{i}(\omega_i^\varepsilon t + \pi/4)}}{(2\pi)^{3/2}R' P^{1/2}\omega_i^\varepsilon(\omega_i^\varepsilon t)^{1/2}}, \tag{59}$$

and the vertical displacement is

$$\xi^{1/2} = 2\mathrm{Re}\,\frac{-(\mathrm{i}\omega_i^\varepsilon/\omega_-)\mathrm{i}(z+\varepsilon\varrho)(f^2+\omega_-^2)(N^2+\omega_-^2)^{1/2}\mathrm{e}^{-\omega_r t + \mathrm{i}(\omega_i^\varepsilon t + \pi/4)}}{(2\pi)^{3/2}R'^3 P^{3/2}\omega_i^{\varepsilon 3}}(\omega_i^\varepsilon t)^{1/2}. \tag{60}$$

The complex function P is defined in the Appendix (A 31). It is very tedious to determine the higher-order corrections and no transparent error estimates can be provided. In the limit $\varepsilon \to 0$ it is found that $P \to 1$, $R' \to R$ and $\mathrm{i}(\omega_i^\varepsilon/\omega_-) \to 1$ ($\omega_- \to \mathrm{i}\omega_i$ and $\omega_r \to 0$). The expressions (41), (42) and (47) for the Green's functions are recovered and amplitudes grow without limit. For the finite-sized forcing the velocity field and displacement amplitude is proportional to $t^{1/2}\exp(-\omega_r t)$ and since

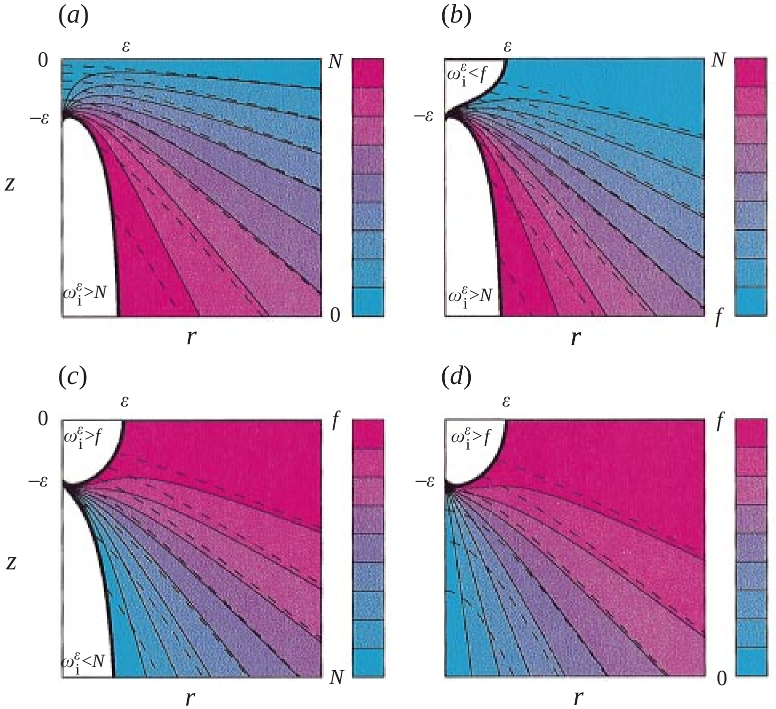

FIGURE 13.

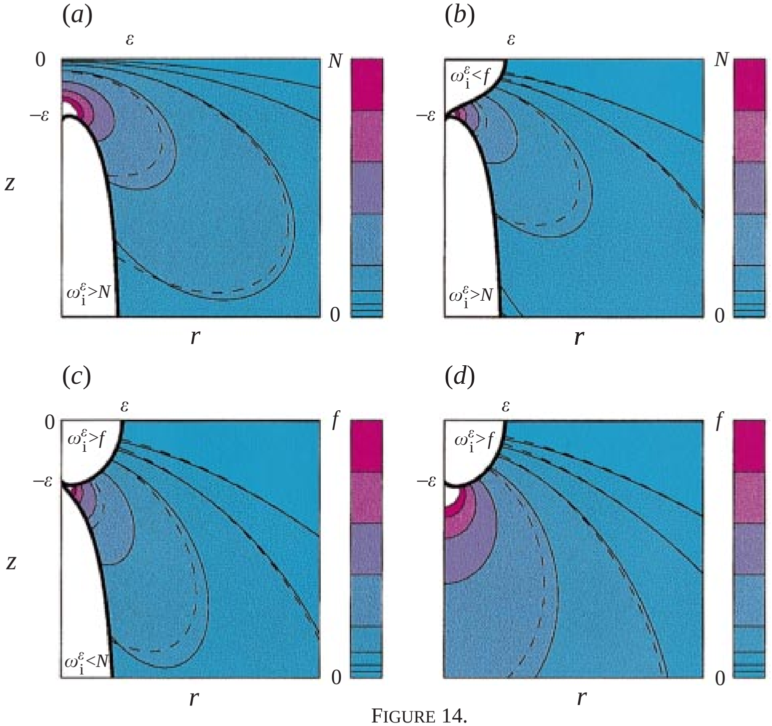

FIGURE 14.

FIGURE 13. Contours of ω_i^ε (solid lines) and the far-field approximation ω_i' (dashed lines) given by (57) for (*a*) $f = 0$, (*b*) $N = 2f$, (*c*) $f = 2N$ and (*d*) $N = 0$. Colouring indicates frequency. Empty regions are where ω_i^ε lies outside the natural frequency range of freely propagating waves. For large distances from the forcing ($r, z \gg \varepsilon$) both ω_i^ε and ω' approach ω_i defined by (15) and are there constant on straight lines $\theta = \text{constant}$.

FIGURE 14. Contours of ω_r (solid lines) and the far-field approximation (dashed lines) given by (57) for (*a*) $f = 0$, (*b*) $N = 2f$, (*c*) $f = 2N$ and (*d*) $N = 0$. Colouring indicates magnitude of ω_r. No contours for $\omega_r > N$ are shown in (*a*) and (*b*), none for $\omega_r > f$ in (*c*) and (*d*). High values of ω_r near the forcing region imply a rapid disappearance of internal waves.

$\omega_r > 0$ for finite ε and $z < 0$, the response is an internal wave *pulse*. That is, at a fixed position first growth occurs, roughly with $t^{1/2}$, which peaks at $t_{\max} = 1/(2\omega_r)$ after which the amplitudes decay. Note that $p^{-1/2}$ is not in phase with $u_r^{1/2}$ and $w^{1/2}$ as for the point forcing. Also $u_\phi^{1/2}$ and $\xi^{1/2}$ are no longer exactly 90° out of phase with $u_r^{1/2}$ and $w^{1/2}$, and $u_r^{1/2}$ and $w^{1/2}$ are not in phase with each other which implies that the radial pulsation character of the response is lost. In the (r, z)-plane the velocity vector is elliptically polarized. Since $\{|u_r^{1/2}|, |u_\phi^{1/2}|, |w^{1/2}|\} \propto \{\omega_i^\varepsilon r, |\omega_i^\varepsilon/\omega_-|fr, \omega_i^\varepsilon|(z + \varepsilon\varrho)|\}$ the polarization relations do not hold.

Defining

$$A = \frac{(f^2 + \omega_-^2)(N^2 + \omega_-^2)^{1/2}}{P^{3/2}} = |A|\mathrm{e}^{\mathrm{i}\phi_A},$$

we find, after a great deal of effort, that

$$\tfrac{1}{2}(u_r^{1/2})^2 = \left(\frac{t\mathrm{e}^{-2\omega_r t}|A|^2}{(2\pi)^3 R'^6 \omega_i^{\varepsilon 3}}\right)\frac{r^2 + \varepsilon^2}{1 + \delta_1^2}[1 + \cos 2\varphi], \tag{61}$$

$$\tfrac{1}{2}(w^{1/2})^2 = (\cdots)\frac{z^2}{1 + \delta_1^2}\left[1 + \cos 2\varphi + \frac{2\delta_1 \sin 2\varphi}{1 + \delta_1^2} - \frac{2\delta_1^2 \cos 2\varphi}{1 + \delta_1^2}\right], \tag{62}$$

$$\tfrac{1}{2}(u_\phi^{1/2})^2 = (\cdots)\frac{f^2(r^2 + \varepsilon^2)}{(1 + \delta_1^2)|\omega_-^2|}\left[1 - \cos 2\varphi - \frac{2\delta_2 \sin 2\varphi}{1 + \delta_2^2} + \frac{2\delta_2^2 \cos 2\varphi}{1 + \delta_2^2}\right], \tag{63}$$

and

$$\tfrac{1}{2}N^2(\xi^{1/2})^2 = (\cdots)\frac{N^2 z^2}{(1 + \delta_1^2)|\omega_-^2|} \times \left[1 - \cos 2\varphi - \frac{2(1 - \delta_1\delta_2)(\delta_1 + \delta_2)\sin 2\varphi}{(1 + \delta_1^2)(1 + \delta_2^2)} + \frac{2(\delta_1 + \delta_2)^2 \cos 2\varphi}{(1 + \delta_1^2)(1 + \delta_2^2)}\right], \tag{64}$$

where

$$\varphi = \omega_i^\varepsilon t + \pi/4 + \phi_A, \quad \delta_1 = \varepsilon/r, \quad \delta_2 = \omega_r/\omega_i^\varepsilon. \tag{65}$$

The terms $(\cdots)$ in (62)–(64) are the same as the first term in (61). When we let $\varepsilon = 0$ in these expressions, add them all up and multiply by $R^2 \sin\theta$ we get the energy density $W' = tF$, i.e. (49), with F as in (44). When $\varepsilon \neq 0$ things do not add up as neatly as in § 4.2.2. The reason is that the phase relations are altered by the terms containing δ_1 and δ_2 in the various expressions in square brackets in (61)–(64). Also the factors between $(\cdots)$ and the terms in square brackets are more complicated than when $\varepsilon = 0$. But, the time-dependent cosines and sines in these expressions represent oscillations about time-dependent, non-oscillatory parts which are the factors preceding the square-bracketed terms. These oscillations do not contribute to the growth in an averaged sense (averaged over an oscillation period). In § 4.2.2 the correct wave energy density (49) would also have been found by putting $\cos 2\varphi = 0$ in (45), (46) and (48) before adding them. Similarly, the average wave energy density for the finite-sized forcing is obtained by setting the cosines and sines in (61)–(64) equal to zero, adding them and multiplying by $R^2 \sin\theta$. This gives

$$W' = t\mathrm{e}^{-2\omega_r t}\left[1 + \frac{\omega_i'^2}{|\omega_-|^2}\right]\frac{|f^2 + \omega_-^2|^2|N^2 + \omega_-^2||N^2 - \omega_i^2|^{1/2}R^2}{(1 + \delta_1^2)(2\pi)^3|P|^3|N^2 - f^2|^{1/2}\omega_i^{\varepsilon 3}R'^4}. \tag{66}$$

In the limit $\varepsilon = 0$ this reduces to (49).

The decay rate ω_r is large in regions underneath the forcing. There, formally, amplitudes peak early and waves rapidly disappear. However, since we are using a large-time expansion, the leading-order behaviour is not reliable because the $O(t^{-1/2})$-correction may not be small at early times. We focus therefore on the behaviour far from the forcing and at large times.

An example of how W' evolves in the (r, z)-plane is shown in figure 15. This case with $N = 2f$ is representative for all cases with $N \neq 0$. The domain is large compared to the forcing size, i.e. the main boxes have dimensions $10^3\varepsilon \times 10^3\varepsilon$ but the smaller boxes show the evolution in a domain of size $10^2\varepsilon \times 10^2\varepsilon$. Non-dimensional times start at $ft = 100$. The white line is a cone at the angle $\theta_{\max} = 0.27\pi$ defined in §4.2.2 along which the energy flux is maximal for the point forcing (see figure 10*b*). As time progresses wave energy rapidly disappears in the smaller domain near the forcing. There the decay rate ω_r is relatively large, as figure 14 indicates. Near the surface, wave energy does not diminish as rapidly as further down because ω_r is smaller near the surface. Essentially the same events occur in the larger domain but at later times. At early times in this sequence we see in the far field a tendency for the wave energy to be symmetric about the maximum flux direction for the point source/sink. Energy clearly propagates outwards but an asymmetric distribution is eventually established. The asymmetry is a consequence of the decay rates ω_r underneath the maximum flux axis being higher than above it. For larger N/f ratios wave energy propagates more in the horizontal, in accordance with the results of §4.2.2. In the limit $f = 0$ (stratified fluid) energy propagates roughly along the axis $\theta_{\max} = \pi/3$ as in figure 10(*a*). Similar energy distributions as in figure 15 are found, but rotated slightly upwards. When N/f becomes smaller the energy distribution patterns rotate downwards. In the limit $N \rightarrow 0$ (rotating homogeneous fluid) energy propagates along the vertical. This is illustrated in figure 16. Only in this limit does the energy density distribution remain symmetric about the maximum flux direction for point forcing, i.e. the vertical axis $r = 0$. As in figure 15 the wave energy disappears in an ever expanding region, initially rapidly near the forcing because the decay rate ω_r is large there (figure 14*d*). There is again a propagating pulse, with highest amplitudes along the vertical.

In figure 17(*a*) we show how W' varies with time at the three positions marked by dots in figure 15. They lie on the maximum-flux cone $\theta_{\max} = 0.27\pi$. It is seen that further away from the forcing the pulse peaks later. This is easily understood and physically trivial. The peak occurs according to (66) at $t_{\max} = 1/(2\omega_r)$. For larger distances from the source ω_r becomes smaller. If we rotated the measuring positions by some angle $\mathrm{d}\theta$ upwards, maintaining the same distance R from the centre of the forcing, we would observe the peaks at later times because ω_r becomes smaller at each position, while rotated downwards at earlier times. The peak amplitude diminishes with the distance from the forcing and closer to the forcing there is a more rapid pulse than further away. Figure 17(*b*) shows how the energy density varies along the maximum-flux cone at different times. We show it as a function of r and not as a function of R, but the graph would have been the same since $r = R \sin\theta_{\max}$. At early times the maximum amplitude of the wave energy in figure 17(*b*) is higher than at later times. This is also clearly seen in figure 15. This is a consequence of energy conservation: as time progresses wave energy spreads out over space and consequently amplitudes decay.

Clearly the results presented here are for the far field where a good approximation to (66) is

$$W' \approx t\mathrm{e}^{-2\omega_r t} F, \tag{67}$$

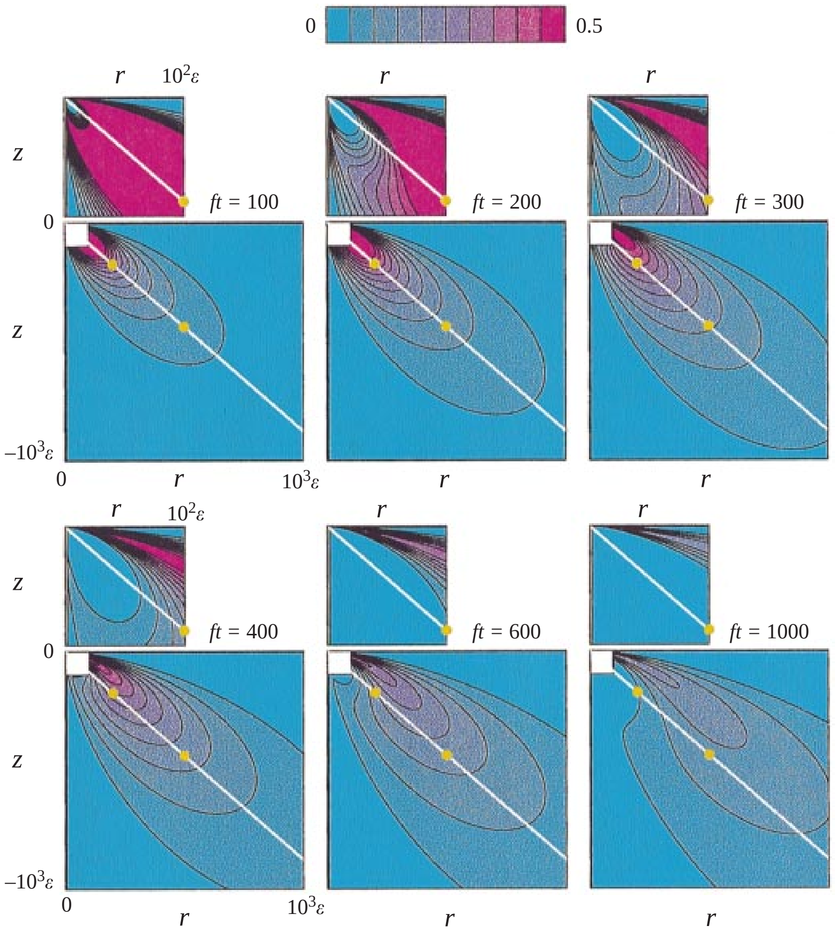

FIGURE 15. Evolution of wave energy density W' given by (66) for $N = 2f$ in response to the forcing $w_s = S(r;\varepsilon)\delta(t)$, normalized by the maximum $W'_{\max}$ of W' that occurred at the earliest time shown ($ft = 100$). Contours are limited to values between 0 and 50% of the maximum of W' at $ft = 100$. All values higher than $0.5W'_{\max}(ft = 100)$ are the same colour. The white line is the ray of maximum energy flux for the point forcing ($\varepsilon = 0$) shown in figure 10(*b*) ($\omega_i = 1.52f$ or $\theta_{\max} = 0.27\pi$). Yellow dots are 'measuring' positions for figure 17(*a*). Times are as indicated. For a further description see text.

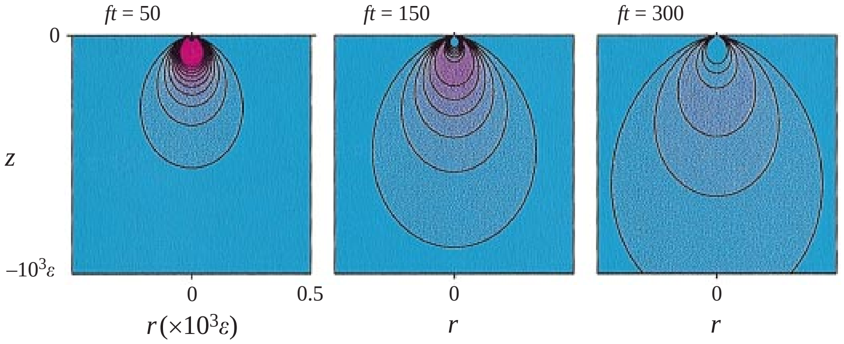

FIGURE 16. Evolution of wave energy density W' given by (66) for $N = 0$ in response to the forcing $w_s = S(r;\varepsilon)\delta(t)$, normalized by the maximum $W'_{\max}$ of W' that occurred at the earliest time shown ($ft = 50$). Contours are limited to values between 0 and 50% of the maximum of W' at $ft = 50$. All values higher than $0.5W'_{\max}(ft = 50)$ have been given the same colour. Times are as indicated.

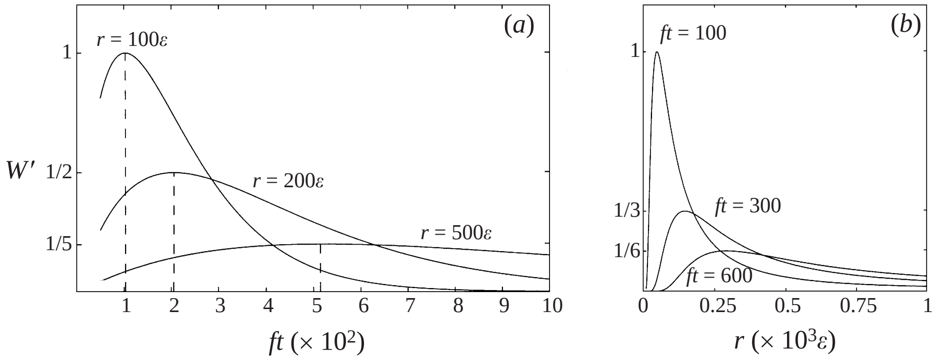

FIGURE 17. (*a*) Evolution of wave energy density at the three 'measuring points' shown in figure 15 ($r = 100\varepsilon$, 200ε and 500ε) and (*b*) wave energy distribution along the maximum flux ray at times $ft = 100$, $ft = 300$ and $ft = 600$. In (*a*) dashed vertical lines mark the time $t_{\max}$ when the pulse peaks at each position. In (*a*) amplitudes have been normalized by the peak amplitude that occurs at $r = 100\varepsilon$, and in (*b*) by the maximum amplitude that occurs along the ray at $ft = 100$. Numbers along the vertical axis indicate the value of the maximum of each curve (to within a fraction of a percent).

with F given by (44) and ω_r approximated by (57). In the far field the time $t_{\max}$ when the pulse peaks at a given observer position and the amplitude of the peak are

$$t_{\max} = \frac{1}{2\omega_r} \approx \frac{\omega_i|N^2 - f^2|^{1/2}}{2|f^2 - \omega_i^2||N^2 - \omega_i^2|^{1/2}}\frac{R}{\varepsilon}, \quad W'(t_{\max}) \approx \frac{|f^2 - \omega_i^2||N^2 - \omega_i^2|}{\mathrm{e}(2\pi)^3\omega_i^2}\frac{1}{\varepsilon R}. \tag{68}$$

The arrival time of the peak is proportional to the distance R from the forcing. Its amplitude depends on the angle θ or ω_i but is otherwise inversely proportional to R. The $t_{\max}$ have been marked in figure 17(*a*) by the dashed vertical lines, and the $W'(t_{\max})$ values, relative to the value at the measuring point closest to the forcing, have been marked on the vertical axis. Figure 17(*a*) shows that in the far field the arrival times are indeed proportional to the distance from the forcing and the peak amplitudes inversely proportional to R, both to within a fraction of a percent. The far-field approximation is therefore very good at these distances from the forcing. In figure 17(*b*) the peaks occur at positions $r_{\max}$ that shift outwards with time. The distance $R_{\max}(t)$ along a ray ω_i = constant where this peak occurs is for the far field derived from (67) by solving $\partial_R W' = 0$. With that determined one can calculate $W'(R_{\max}(t))$, i.e. how the shifting peak decays with time. The solution is

$$\begin{aligned} R_{\max}(t) &\approx \frac{\varepsilon|f^2 - \omega_i^2||N^2 - \omega_i^2|^{1/2}}{\omega_i|N^2 - f^2|^{1/2}}t, \\ W'(R_{\max}(t)) &\approx \frac{|N^2 - f^2|^{1/2}|f^2 - \omega_i^2||N^2 - \omega_i^2|^{1/2}}{\mathrm{e}^2(2\pi)^3\omega_i}\frac{1}{t}. \end{aligned} \tag{69}$$

Thus, the peak moves along a ray of constant ω_i with a *constant speed* and decays with t^{-1}. In figure 17(*b*) the $W'(R_{\max}(t))$ values relative to the value at the earliest time ($ft = 100$) have been marked on the vertical axis. It is found that to within a fraction of a percent the peak amplitudes decay with t^{-1}. This is another confirmation that the far-field approximation is very good at these distances from the forcing. We also compared the graphs shown in figure 15 directly with graphs of the energy density evolution in the far-field approximation, i.e. (67) with ω_r approximated by (57). But for small differences near the forcing, they were indistinguishable.

With the far-field expressions we can determine what the total wave energy is as a function of θ or ω_i. If we integrate W' given by (67) from $R = R_1$ to $R = \infty$ and over the azimuthal angle ϕ we get

$$E_i(R > R_1, \theta, t) = \int_{R_1}^{\infty} \int_0^{2\pi} W' \, \mathrm{d}\phi \, \mathrm{d}R = \frac{|f^2 - \omega_i^2(\theta)||N^2 - \omega_i^2(\theta)|}{\varepsilon(2\pi)^2 \omega_i^2(\theta)} [1 - \exp(-2\gamma t/R_1)], \tag{70}$$

where

$$\gamma = \frac{\varepsilon |f^2 - \omega_i^2(\theta)||N^2 - \omega_i^2(\theta)|^{1/2}}{\omega_i(\theta)|N^2 - f^2|^{1/2}} \tag{71}$$

comes from writing $\omega_r \approx \gamma/R$ for the far-field approximation (57). This is the energy density in θ-space so that the total energy outside a hemisphere of radius R_1 at a given time is $\int_0^{\pi/2} E_i(R > R_1, \theta, t) \, \mathrm{d}\theta$. In frequency space the density is

$$E_i(R > R_1, \omega_i, t) = \frac{|f^2 - \omega_i^2|^{1/2}|N^2 - \omega_i^2|^{1/2}}{\varepsilon(2\pi)^2 \omega_i} [1 - \exp(-2\gamma t/R_1)], \tag{72}$$

and the total energy is then $\int E_i(R > R_1, \omega_i, t) \, \mathrm{d}\omega_i$ with integration over the range of values ω_i can take. In figure 18(a) we show how $E_i(R > R_1, \omega_i, t)$ evolves with time when $N = 2f$. For R_1 we took the radius R corresponding to the observer position at $r = 100\varepsilon$ on the maximum-flux cone $\theta_{\max} = 0.27\pi$. At early times E_i is roughly symmetric about the maximum-flux frequency for the point forcing, in accordance with figure 15. As time progresses the peak in the energy distribution shifts towards lower frequencies. This corresponds to the upward shift of the patterns in figure 15. If we normalize the energy distribution at each time with the total energy $\int E_i \, \mathrm{d}\omega_i$, we find that energy is not conserved in a given frequency band but spreads to neighbouring frequency bands. After $ft = 1000$, $E_i(R > R_1, \omega_i, t)$ in figure 18(a) barely changes anymore. At this point almost all wave energy has propagated beyond $R = R_1$. In the last panel of figure 15 there is still a narrow band of relatively high wave energy in the domain with $r < 100\varepsilon$ but because it is so narrow both in terms of the range of θ or ω_i its total energy is very small compared to what has propagated out of this domain. By letting $t \to \infty$ in (70), we obtain the wave-energy distribution

$$E_i(\theta) = \frac{|f^2 - \omega_i^2(\theta)||N^2 - \omega_i^2(\theta)|}{\varepsilon(2\pi)^2 \omega_i^2(\theta)}, \quad E_i(\omega_i) = \frac{|f^2 - \omega_i^2|^{1/2}|N^2 - \omega_i^2|^{1/2}}{\varepsilon(2\pi)^2 \omega_i}. \tag{73}$$

It follows from (73) that the wave-energy distribution has a maximum at $\omega_i = \omega_{\max} = (Nf)^{1/2}$. Figure 18($a$) shows that at $ft = 1000$ the peak energy occurs very close to this frequency ($\omega_i = \sqrt{2}f$).

In figure 18(b) we show the evolution of wave energy for the stronger stratification $N = 10f$. The maximum-flux cone for the point forcing is at an angle $\theta_{\max}$ close to $\pi/3$. For R_1 we took the radius R where the maximum-flux cone is at $r = 100\varepsilon$. Time is measured in inertial periods and because the stratification is stronger than in the case of figure 18(a), things evolve faster. Again a shift of wave energy towards f with increasing time is observed. For large times the peak approaches $\omega_i = (Nf)^{1/2} = \sqrt{10}f$. In the limit $f \to 0$, or $N/f \to \infty$, the maximum occurs at $\omega_i = 0$, i.e. the horizontally propagating zero-frequency waves in the far field are the most energetic in a stratified fluid. In the limit $N \to 0$ the maximum also occurs at $\omega_i = 0$, i.e. the vertically propagating zero-frequency waves in the far field are the most energetic in a rotating homogeneous fluid. The far-field approximation has been found to be still very good at distances ten times smaller than used in figure 18. With $R_1 = O(10\varepsilon)$ the final wave

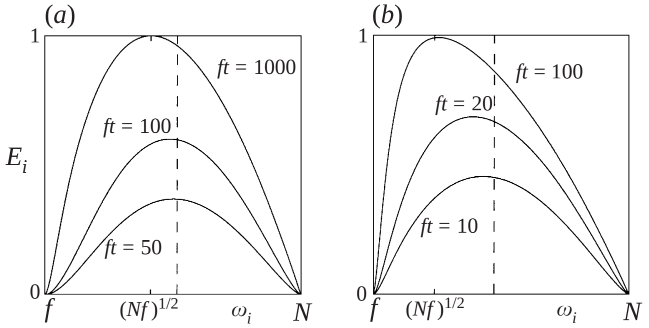

FIGURE 18. Evolution of wave energy density $E_i(R > R_1, \omega_i, t)$ given by (72) for (*a*) $N = 2f$ and (*b*) $N = 10f$. It gives all the wave energy outside a hemisphere of radius R_1 placed about the centre of the forcing $w_s = S(r;\varepsilon)\delta(t)$. $R_1 = 133\varepsilon$ in (*a*), $R_1 = 117\varepsilon$ in (*b*) (see text). Dashed lines indicate the frequency at which the energy density and flux for the point forcing is maximal, (*a*) $1.52f$ and (*b*) $5.2f$. For large time ($ft = 1000$ in (*a*), $ft = 100$ in (*b*)) almost all waves have propagated out of the hemisphere and the final wave energy distribution (73) is established. It has a maximum at $\omega_i = \sqrt{Nf}$.

energy distribution is established about ten times earlier. For $N = 2f$ (figure 18*a*) this would be at roughly $ft = 100$, for $N = 10f$ (figure 18*b*) it would be at about $ft = 10$.

The total wave energy E_i is $\int_0^{\pi/2} E_i(\theta)\,\mathrm{d}\theta$ or $\int E_i(\omega_i)\,\mathrm{d}\omega_i$. For example

$$N = 0: \quad E_i = \frac{1}{\varepsilon(2\pi)^2}\int_0^{\pi/2} |f^2 - \omega_i^2(\theta)|\,\mathrm{d}\theta$$

$$= \frac{1}{\varepsilon(2\pi)^2}\int_0^{f} |f^2 - \omega_i^2|^{1/2}\,\mathrm{d}\omega_i = \frac{1}{4}\frac{f^2}{4\pi\varepsilon} = E_k(0), \tag{74}$$

$$f = 0: \quad E_i = \frac{1}{\varepsilon(2\pi)^2}\int_0^{\pi/2} |N^2 - \omega_i^2(\theta)|\,\mathrm{d}\theta$$

$$= \frac{1}{\varepsilon(2\pi)^2}\int_0^{N} |N^2 - \omega_i^2|^{1/2}\,\mathrm{d}\omega_i = \frac{1}{4}\frac{N^2}{4\pi\varepsilon} = E_p(0). \tag{75}$$

In (74) $E_k(0)$ is the kinetic energy of the initial vortex (see §4.3), in (75) $E_p(0)$ is the potential energy stored in the initial vertical displacement field. As discussed in §4.3 we expected in these two cases all of the initial energy to be converted to wave energy, because in neither case an asymptotic vortex remained. The integral for E_i in the general case is much harder but can be evaluated exactly and we find (54) again. The conclusion is therefore that energy is conserved if the total energy of the $O(t^{1/2})$ wave field is added to the remaining energy stored in the asymptotic vortex.

4.4.2. *Buoyancy oscillations*

To leading order the velocity components of the buoyancy oscillations are

$$w_s = S(r;\varepsilon)\delta(t): \quad \{u_r, u_\phi, w\} = 2\mathrm{Re}\,\frac{\{Nr, \mathrm{i}fr, Nz\}N\mathrm{e}^{\mathrm{i}(Nt-\pi/4)}}{(2\pi)^{3/2}(r^2+\varepsilon^2)^{3/2}(N^2-f^2)^{1/2}}$$

$$\times\frac{1}{(Nt)^{3/2}}[1 + O((Nt)^{-1}) + O(t_N'^{-1})], \tag{76}$$

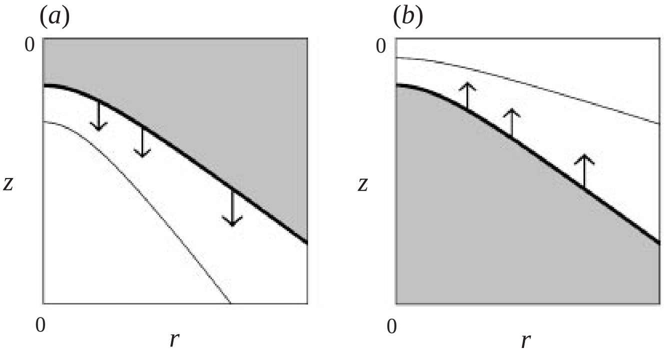

FIGURE 19. Regions of validity (shaded areas) of the leading-order behaviour for a given degree of precision of (*a*) the buoyancy oscillations given by (76) and (77) and (*b*) the inertial oscillations given by (78) and (79). With increasing time in (*a*) the region expands downwards, in (b) upwards (see text).

$$w_s = S'(r;\varepsilon)\delta(t): \quad \{u_r, u_\phi, w\} = 2\mathrm{Re}\,\frac{\{Nr, \mathrm{i}fr, Nz\}3\varepsilon N \mathrm{e}^{\mathrm{i}(Nt-\pi/4)}}{(2\pi)^{3/2}(r^2+\varepsilon^2)^{5/2}(N^2-f^2)^{1/2}} \times \frac{1}{(Nt)^{3/2}}[1 + O((Nt)^{-1}) + O(t_N'^{-1})]. \tag{77}$$

Here $t'_N = |N^2 - \omega_i'^2|t/N$. Note that (77) $= -\partial_\varepsilon$(76). When we let $\varepsilon \to 0$ in (76) the result for the Green's function (40) is recovered. With finite ε amplitudes are well-behaved everywhere. In the first case the horizontal velocity amplitude decays with r^{-2} for large r and in the second case with r^{-4}, but the decay rates with time are the same. Assuming $Nt \gg 1$, the leading-order behaviour for both cases is also valid when $t'_N \gg 1$ and the situation is as in §4.2.1: there are *horizontal* velocities varying with the buoyancy frequency, radial oscillations along lines θ =constant, and with increasing time the horizontal velocity amplitude becomes depth-independent in areas where $t'_N \gg 1$. For a given tolerably small error δ, determined by a fixed large value of t'_N, it follows that errors smaller than δ are found in an increasingly larger region between the upper surface $z = 0$ and a surface defined by $\omega'_i = C(t)$, which is the grey area in figure 19(*a*). The arrows indicate how this area expands with time.

4.4.3. *Inertial oscillations*

For $w_s = S(r;\varepsilon)\delta(t)$ inertial oscillations are part of the response with velocity components

$$\{u_r, u_\phi\} = 2\mathrm{Re}\,\frac{9\varepsilon r}{z^4}\,\frac{\{f, \mathrm{i}f\}f^3\mathrm{e}^{\mathrm{i}(ft+3\pi/4)}}{(2\pi)^{3/2}(N^2-f^2)^{3/2}(ft)^{5/2}}[1 + O((ft)^{-1}) + O(t_f'^{-1})], \tag{78}$$

and

$$w = 2\mathrm{Re}\,\frac{6\varepsilon}{z^3}\,\frac{\{f\}f^3\mathrm{e}^{\mathrm{i}(ft+3\pi/4)}}{(2\pi)^{3/2}(N^2-f^2)^{3/2}(ft)^{5/2}}[1 + O((ft)^{-1}) + O(t_f'^{-1})], \tag{79}$$

with $t'_f = |\omega_i'^2 - f^2|t/f$. Unlike the buoyancy oscillations, they disappear when the size of the forcing shrinks to zero ($\varepsilon \to 0$). They decay rapidly in the vertical, which indicates that they are surface-confined. They have a fleeting existence: they decay with $t^{-5/2}$ whereas the buoyancy oscillations decay with $t^{-3/2}$. Note that these inertial oscillations have a non-zero *vertical* velocity component. There are radial oscillations along lines θ = constant plus an azimuthal flow slaved to u_r through $\partial_t u_\phi = -f u_r$. We cannot let $z \to 0$ in these expressions because $\omega_i' \to f$ as $z \to 0$, and $t_f'^{-1} \to \infty$. The leading-order behaviour holds for a given time and a given degree of precision in regions underneath an ω_i' = constant surface. This is sketched in figure 19(*b*). For increasing time the region of validity of (78) and (79) shifts towards the surface.

5. Discussion

The purpose of this paper has been to develop insight into the response of a rotating stratified fluid to surface forcing of the kind sketched in the introduction. An overview of the main results, open questions and other matters of possible interest follow now. First we note that the Green's functions in § 2 for arbitrary combinations of N and f for the particular problem studied here appear new. They differ by a factor 2 from the Green's functions for internal point sources in a fluid of infinite extent in all directions. This is because the Green's function(s) for the semi-infinite domain with a rigid upper lid can be constructed from that for the infinite domain by placing two point sinks symmetrically on either side of the surface and then letting them approach each other. For $f = 0$ our result reduces to that of Dickinson (1969) for a point source/sink in a stratified fluid of infinite extent. He derived a Green's function for a scalar W from which through differentiation the velocity fields and pressure can be determined, which he did not do. Our h (14) coincides when $f = 0$ with his W except for the factor 2. Dickinson derived the complete asymptotic series of h_N, h_i for $f = 0$ and the leading-order term in (38) is, besides the factor 2, the same as his (f enters in our expression through the definition of ω_i). Different representations using special functions have been derived for $f = 0$ by Gordeichik & Ter-Krikorov (1996). We expressed the Green's functions in terms of two scalar fields ψ and h which are related to each other: $\psi = \partial_t h(\cdots;t) + N^2 \int_0^t h(\cdots;t')\,\mathrm{d}t'$. This is not obvious if one considers (14) but follows easily from (A 12) in the Appendix. Upon combining (18) with the expression for G_w in (13), it follows that the velocity field is determined by h alone according to

$$\boldsymbol{u} = (G_u, G_v, G_w) = \partial_t^2 \nabla h + N^2 \nabla_{\mathrm{h}} h + \boldsymbol{z} f^2 \partial_z h + f \nabla_{\mathrm{h}} \wedge \boldsymbol{z} \times \left[\partial_t h(\cdots;t) + N^2 \int_0^t h(\cdots;t')\,\mathrm{d}t' \right].$$

For $N = 0$ this reduces to the example Hart (1981) gave for a homogeneous rotating fluid (he did not calculate h though); for $f = 0$ it becomes the expression Voisin (1991) gives for a stratified fluid (where our h is called ψ). The velocity field due to the finite-sized forcings can also be expressed in this fashion in terms of a single scalar potential h, but to see this the Appendix needs to be consulted.

For each of the impulsive forcings the first stage in the dynamics is potential flow followed when $f \neq 0$ by the formation of a vortex (§ 3.1–§ 3.4). Physically it is easily understood why cyclones or anticyclones form, depending on the sign of the forcing (suction or pumping). In each case an unbalanced initial condition is created and adjustments follow. The $O(t)$-adjustments are the leading-order behaviour of the transient internal wave field. Somewhat surprising is that the streamline patterns (figure 8) are independent of the value of N/f while flow directions do depend on the value of N/f. These $O(t)$-adjustments in the axial plane lead to changes in the vortices. Remarkably, (§ 4.1) asymptotically the vortices become self-similar to what they were initially, according to the scaling $z \to (N/f)z$. How this comes about is not clear. It is also remarkable (§ 4.3) that for *both* finite-sized forcings the asymptotic vortices have their energy equally divided between potential and kinetic energy whereas initially $E_p/E_k = (N/f)^2$ and that in both cases the same fraction of the total initial energy goes to the waves and oscillations although the initial conditions are quite different. It is unlikely that this is always true for initial conditions such that asymptotically a vortex or geostrophically balanced current remains but it is intriguing. When $f = 0$ all initial potential energy goes to the waves and oscillations (there is no kinetic energy, i.e. no initial vortex), whereas for increasingly smaller $N < f$ with fixed $f \neq 0$ more and more of the initial energy is converted into waves and oscillations and the vortex becomes more stretched in the vertical. For fixed $f \neq 0$ and increasing $N > f$ the vortex becomes more compressed in the vertical and more energy goes again to the waves. This may seem surprising because for large N a stronger vortex remains. Inspection of (53) shows that when $N > f$ the final vortex has indeed more kinetic energy than initially. But, more potential energy is released than needed to make up for the kinetic energy deficit, and for increasing N the energy surplus becomes larger. For $N > f$ we could say that the waves' energy comes from a release of potential energy. Vice versa, when $N < f$ potential energy increases while the kinetic energy decreases and the waves' energy comes from a release of kinetic energy. In the limit $N = 0$ the vortex disappears. A simple argument can explain this for the finite-sized forcings: an infinitely long, depth-independent vortex has infinite total energy. This is impossible to create with injection or suction of a finite volume of fluid with a finite-amplitude velocity distribution at the surface. A Taylor column can only be established with such forcing in a fluid layer of finite depth.

An attempt to isolate the vortices' evolution from the wave field failed. Since linear internal waves carry no linearized Ertel potential vorticity $q(\boldsymbol{x};t) = \omega_z(\boldsymbol{x};t) - f\int_0^t \partial_z w(\boldsymbol{x};t'')\,\mathrm{d}t''$, where $\omega_z = \nabla_{\mathrm{h}} \wedge \boldsymbol{u}_{\mathrm{h}}$, $\boldsymbol{x} = (x,y,z)$, it appeared that if these operations were applied to the fields, internal waves would become 'invisible' and only the vortices would remain. But, it can be shown that the vortices also have $q = 0$ at all times. The explanation is that all initial relative vertical vorticity ω_z is created through vortex tube stretching/compression by the potential flow, i.e. $\omega_z = f\partial_z\xi$, with ξ the vertical displacement $\xi = \int_0^t w(t')\,\mathrm{d}t'$ and $q = 0$ everywhere initially and afterwards. This illustrates that transient internal wave fields can create zero-potential-vorticity carrying geostrophic currents or vortices in a rotating fluid: consider a location where a circularly symmetric wave packet passes through. The radial velocity u_r is proportional there to $A(t)\cos(\omega_i t + \phi)$ where $A(t)$ is the envelope of the wave packet and ω_i the frequency and ϕ an arbitrary phase. The azimuthal velocity v is determined by the equation $\partial_t v = -fu_r$ and after the wave packet has passed by $v(t=\infty) = v(0) - f\int_0^\infty u(t')\,\mathrm{d}t'$, with $v(0)$ the initial azimuthal velocity. If we take for example $A(t) = t\exp(-\alpha t)$

$$v(t=\infty) = v(0) + f\,\frac{(\omega_i^2 - \alpha^2)\cos\phi + 2\alpha\omega_i\sin\phi}{(\alpha^2+\omega_i^2)^2}.$$

Depending on whether $\alpha > \omega_i$ (a rapid pulse) or $\alpha < \omega_i$ (a slow pulse) and on the phase ϕ, $v(\infty)$ can be either smaller or larger than $v(0)$. This is not very different from the Rossby adjustment problem (Gill 1982) where the evolution of a free-surface displacement is studied for a homogeneous rotating fluid. It is invariant in the y-direction. The Coriolis force acting on the velocity component u in the x-direction leads ultimately to steady geostrophic flow v in the y-direction.

In § 4.2.2 we established for the point-forcing how the flux of internal wave energy depends on N/f. For $N = 0$ the maximum flux is in the vertical (figure 10), which corresponds to the maximum group velocity direction according to (5). For $f = 0$ however the flux is maximal in a direction that makes an angle $\theta = \pi/3$ with the vertical, which is not the maximum group velocity direction. This result can heuristically be explained for the point forcing as follows: the Fourier spectrum of the initial vertical displacement field $\xi = -z/2\pi R^3$ is $\tilde{\xi} = 2\mathrm{i}m/|\boldsymbol{k}|^2$. Introducing the angle θ with the vertical again, we have $\tilde{\xi} = 2\mathrm{i}\sin\theta/|\boldsymbol{k}|$. Switching to spherical coordinates in wavenumber space the potential energy density is $N^2\tilde{\xi}\tilde{\xi}^\star|\boldsymbol{k}|^2\cos\theta\,\mathrm{d}|\boldsymbol{k}|\,\mathrm{d}\theta\,\mathrm{d}\phi$ which is proportional to $\sin^2\theta\cos\theta$. Multiplying this by $\boldsymbol{U}_\mathrm{g}$ (i.e. 4) we see that the flux in spectral space varies with $\sin^3\theta\cos\theta$ which for any $|\boldsymbol{k}|$ is maximal for $\theta = \pi/3$ (i.e. $\cos\theta = 1/2$). This argument may be too simple since the evolution cannot entirely be determined by just the spectrum of the initial displacement field, but it points in the right direction. Thus, it appears that the surprise for $f = 0$ is due to the fact that although the group velocity is maximal for $\theta = \pi/2$ (zero-frequency waves), the energy density in wavenumber space vanishes there and the flux is maximal at an intermediate angle.

Studies closest to ours are the one by Bretherton (1967), who studied the response of a homogeneous rotating fluid to the impulsive displacement of an infinitely long horizontal cylinder along the rotating axis, the study by Hendershott (1969) of the response of a stratified rotating fluid to impulsively started oscillations of a sphere, and Voisin's (1991) extensive review article. In the last, results are given for the response of a stratified fluid to an impulsive expansion of a sphere. Absent from these studies is a recognition that to leading order the internal wave field propagates as a pulse, as discussed in §4.4.1. Bretherton finds that for large time at a fixed position the velocity fields decay with $t^{-1/2}$. For large time, but fixed R/t (an observer moving with constant speed), he finds that velocity amplitudes grow with t. Hendershott finds that at a fixed position first amplitudes grow with $t^{1/2}$ and ultimately decay with $t^{-1/2}$. Voisin cites similar results. In all three cases it is clear that a pulse-like wave field should be observed at some distance from the forcing. The initial $t^{1/2}$-growth followed by $t^{-1/2}$-decay does suggest something pulse-like. However, Voisin mentions that for the pulsed sphere the $t^{-1/2}$-decay is found in an ever expanding 'torus'. This must correspond to the expanding low-amplitude regions seen in figures 15 and 16 where the pulse has peaked and the leading-order term has become very small. In these regions the $O(t^{-1/2})$-correction to the internal wave field may dominate. It appears that in this study for the first time a reasonably complete 'global' picture of a propagating internal wave field has been established.

With domain sizes as in figures 15 and 16 the source/sink is almost point-like for an observer. But, even the smallest finite horizontal scale of the forcing is enough to completely alter the response as compared to the response to point forcing. The unbounded growth of amplitudes in the latter case can be accounted for by the infinite energy stored in the initial condition. For the forcing $w_s = S(r;\varepsilon)\delta(t)$ the total initial energy is finite and the wave field is well-behaved. The pulse is best described by the $t^{1/2}\mathrm{e}^{-\omega_r t}$ behaviour of the velocity amplitudes. The far-field approximation of the relevant quantities (57) leading to the approximation (67) for the wave energy density is very good. Analytical expressions describing the propagation of the pulse have been derived and we also determined the global energy spectrum (73) of the internal wave field. The total wave energy is equal to the difference between the energy stored in the initial condition and the energy of the asymptotically remaining vortex. Thus, buoyancy and inertial oscillations, the $O(t^{-1/2})$-correction to the internal wave field, and all higher corrections, asymptotically play no role in the energy budget. They do not propagate, decay algebraically and with time the associated energy becomes negligible.

It is remarkable that the global energy distribution $E_i(\omega_i)$ (73) varies with ω_i just as the group velocity $\boldsymbol{U}_{\mathrm{g}}$ (4) does. It was obtained by integrating over space outside a hemisphere surrounding the forcing region. For $N \neq 0$ the energy density distribution is not symmetric about any particular angle θ or frequency ω_i as seen in for example figure 15. Only far from the forcing is this approximately true, with symmetry about the maximum flux direction for the point forcing. With increasing time the region where symmetry is found moves outwards. The angle about which symmetry is found does not correspond to the frequency where $E_i(\omega_i)$ is maximal when $N \neq 0$. The former is a solution of $\partial_{\omega_i} F = 0$ with F given by (44), the latter a solution of $\partial_{\omega_i} E_i(\omega_i) = 0$. A simple explanation for why E_i and $\boldsymbol{U}_{\mathrm{g}}$ appear to be related has not been found. Above we gave a simple argument explaining why when $f = 0$ for the point forcing the flux or energy density is maximal along the line $\theta = \pi/3$. For the finite-sized forcing the spectrum of the initial vertical displacement field $\xi = (-z + \varepsilon)/2\pi R_\varepsilon^3$ is $\tilde{\xi} = 2\mathrm{i} \sin\theta \mathrm{e}^{-\varepsilon|\boldsymbol{k}|\cos\theta}/|\boldsymbol{k}|$. Now the potential energy density is proportional to $\sin^2\theta\cos\theta \mathrm{e}^{-2\varepsilon|\boldsymbol{k}|\cos\theta}$. If we multiply this by $\boldsymbol{U}_{\mathrm{g}}$ we find that when $f = 0$ the flux in spectral space varies with $\sin^3\theta\cos\theta \mathrm{e}^{-2\varepsilon|\boldsymbol{k}|\cos\theta}/|\boldsymbol{k}|$. It is maximal at an angle θ for which $4\cos^2 - 1 + 2\varepsilon|\boldsymbol{k}|\sin^2\cos = 0$. When $\varepsilon > 0$ the solution depends on $|\boldsymbol{k}|$. For very small $|\boldsymbol{k}|$ it approximates $\theta = \pi/3$. The group velocity is high for small $|\boldsymbol{k}|$ and this explains why at a given time in the far field the density tends to be maximal about the maximum flux angle for the point forcing. For large $|\boldsymbol{k}|$ however the angle approaches $\theta = \pi/2$ ($\cos\theta = 0$). Now the group velocity is small and this is a plausible explanation for why closer to the forcing region at a given time the energy density is highest near the surface, as in figure 15 where $N = 2f > 0$ instead of $f = 0$.

The forcing $w_s = S(r;\varepsilon)\delta(t)$ was chosen for mathematical convenience. The response to forcings that are similar to this one, say a Gaussian distribution, is most likely not very different. The far field for the other finite-sized forcing, $w_s = S'(r;\varepsilon)\delta(t)$, is far more complicated and no thorough investigation has been made of its properties. The propagating part consists to leading order of a component that grows with $t^{3/2}\mathrm{e}^{-\omega_r t}$ and one that grows with $t^{1/2}\mathrm{e}^{-\omega_r t}$. In § 4.1 it was shown that for this forcing the asymptotic vortex is quite different from the vortex for the other forcing. But, in § 4.3 we showed that the same fraction of the initial energy goes to the waves in each case. The wave energy distribution for this complex case is therefore most likely the same function of N, f and ω_i as (73), but the analysis is too involved to prove this.

The observation in § 4.4.1 that the propagating internal wave field does not satisfy the polarization relations may be of interest to oceanographers. In testing energy spectra in the internal wave frequency band for the existence of random ensembles of linear internal waves, the polarization relations are used to derive theoretical expressions that only depend on the frequency. Systematic deviations are found by Olbers (1983) and his conclusion that ‘this systematic disparity from internal wave kinematics points towards a complex contamination process’ may not be correct. Since the oceanic internal wave field is at least partially generated by coherent forcings like in this study, every data set will be ‘contaminated’ by non-random internal waves, a continuum of which can violate the polarization relations.

In § 4.2.1 and § 4.4.2 we showed that non-vertical buoyancy oscillations are a component of the response. For $f = 0$ this was observed by Voisin (1991) for point forcing and forcing by an impulsively expanding sphere in an infinite stratified fluid. The fact that this is not in accord with the properties of plane waves at this frequency (non-vertical oscillations) and contradicts group velocity theory (they are spread throughout space but should not propagate) led to the cryptic remark that 'this testifies to their non-Boussinesq origin'. Since these results are found in a model where the Boussinesq approximation has been made, the explanation should also be found within that framework. That they are non-vertical is not so mysterious if it is realized that for plane waves with the buoyancy frequency the wave vector $\boldsymbol{k}$ is horizontal (see figure 2). That is, the buoyancy oscillations are then depth-independent. If initial conditions are such that vertical buoyancy oscillations are part of the response with amplitudes that vary with depth, then horizontal velocity components are forced to oscillate with the buoyancy frequency too in order that $\nabla \cdot \boldsymbol{u} = 0$. Note that the buoyancy oscillations for the forcing $w_s = S'(r;\varepsilon)\delta(t)$ given by (77) decay more rapidly in the horizontal than for $w_s = S(r;\varepsilon)\delta(t)$, i.e. their horizontal scale is linked with the horizontal scale of the forcings and therefore the vertical displacement fields. A reasonable explanation is therefore the following. The evolution of the initial vertical displacement field, which varies throughout space, is governed by the radiation of internal waves. At frequency N they do not propagate. Since they are depth-dependent they necessarily have horizontal components.

In §4.4.3 the existence of non-horizontal inertial oscillations was noted. Bretherton (1967), in his study of the impulsively displaced cylinder in a rotating fluid, also found inertial oscillations distributed throughout space, but they decayed with $t^{-3/2}$ whereas here they decay with $t^{-5/2}$. He could not find an entirely satisfactory explanation for the development of these motions. The explanation for their non-horizontal character is simple if we allow for the possibility that inertial oscillations are part of the response but with amplitudes that vary in the horizontal (for a plane wave with the inertial frequency the wave vector is vertical and there is thus no variation in the horizontal): the divergence of the horizontal velocity drives a vertical component at the inertial frequency. An explanation for why they are surface-confined in our problem and are absent for the point forcing has not been found.

We have not analysed the evolution of the wave field close to the forcing region, in particular the response in the unphysical regions shown in figure 13. The question is whether there are actually trapped waves outside the natural frequency range or not. With reference to the Appendix, this reduces mathematically to the question of whether when the branch cut at ω_- in figure 23(a) crosses one of the fixed branch cuts there is a contribution to the inverse Laplace transform. With a simple transformation the movable branch points at ω_- and $\omega_-^\star$ can be made fixed stationary phase points. In the plane of the transform variable the steepest descent paths correspond then almost exactly to the horizontal contours C_- and $C_-^\star$ in figure 23. The fixed branch points at $\pm\mathrm{i}N$ and $\pm\mathrm{i}f$ become movable branch points with this transform. The boundary of the unphysical region (thick lines in figures 13 and 14) corresponds to when these branch points lie on the steepest descent path. For smaller ω_r on the boundary (closer to the surface generally and at large depths), these branch points get closer to the stationary phase points. As ω_- and $\omega_-^\star$ move into the unphysical range, the contour can still be deformed into one with segments along the steepest descent paths and it appears therefore that the trapped waves exist. But, the details are complicated and for a thorough investigation advanced techniques like uniformly asymptotic expansions are probably needed (Bleistein & Handelsman 1986; Felsen & Marcuvitz 1972). Physically the existence of these regions with trapped waves outside the natural frequency band and their shape are most likely due to the interference of plane waves propagating towards the axis from all sides. This requires further study.

This research has been supported by Office of Naval Research Grant N00014-96-0762 and by National Science Foundation Grant OCE 97-30843.

Appendix. Mathematical details

A.1. *Green's functions*

For the derivation of the Green's functions in § 2 we must calculate the transforms (12) of the system of equations (11). First consider $\mathscr{L}_z^{-1}w(k,l,s;\omega) = w(k,l,z;\omega)$. Because

$$\frac{1}{|\boldsymbol{A}|} = \frac{1}{2\alpha\omega(\omega^2+f^2)}\left[\frac{1}{s+\alpha} - \frac{1}{s-\alpha}\right], \quad \alpha = \frac{(\omega^2+N^2)^{1/2}}{(\omega^2+f^2)^{1/2}}(k^2+l^2)^{1/2}, \tag{A 1}$$

there are poles at $s = \pm\alpha$. For $z' < 0$ we close the contour in the right-hand side of the complex s-plane and get zero as a result. For $z' > 0$ ($z < 0$, the interior of the fluid) we close in the left-half of the plane, encircling the two poles in positive direction, and get

$$w(k,l,z;\omega) = \frac{(e^{\alpha z'}+e^{-\alpha z'})w_s(k,l;\omega)}{2} + \frac{\omega(k^2+l^2)(e^{\alpha z'}-e^{-\alpha z'})p_s(k,l;\omega)}{2\alpha(\omega^2+f^2)}. \tag{A 2}$$

The question is how the unknown surface pressure term p_s is related to w_s and how to choose branch cuts in the ω-plane for the functions $(\omega^2+N^2)^{1/2}$ and $(\omega^2+f^2)^{1/2}$ that appear in (A 1). Causality only imposes the condition that the cuts cannot run into the right-hand side of the complex ω-plane. The following physical considerations are used. The contour for $\mathscr{L}_t^{-1}$ in the complex ω-plane can be deformed into one along the imaginary axis, with indentations to the right of the singular points. The inverse transform is then a Fourier transform

$$\mathscr{L}_t^{-1}(\cdot) = \frac{1}{2\pi}\int_{-\infty}^{+\infty}(\cdot)e^{i\omega' t}\,d\omega' \quad (\omega' \equiv \omega/i)$$

where $(\cdot)$ stands for (A 2). For a given pair (k,l) (A 2) thus gives the vertical velocity due to surface forcing periodic in the x- and y-directions which oscillates at a frequency ω'. Note that when we write $\alpha = im$ in (A 1), m is the vertical component of the wave vector which for given k,l,ω' satisfies the dispersion relation (3). Consider the case $N > f$ (special case $f = 0$ included). Then for $f < |\omega'| < N$, α given by (A 1) is imaginary, and the terms $e^{\pm\alpha z'}$ in (A 2) are thus 'wavy' in the vertical. This is the frequency range in which the system can support propagating waves. Energy must propagate away from the surface (in the positive z'-direction) and phase propagation must be in the negative z'-direction (radiation condition). If α is negative imaginary for $if < \omega < iN$ and positive imaginary for $-iN < \omega < -if$ then the radiation condition is satisfied if the terms proportional to $e^{\alpha z'}$ in (A 2) vanish, i.e. when

$$p_s(k,l;\omega) = \frac{-\alpha(\omega^2+f^2)}{\omega(k^2+l^2)}w_s(k,l;\omega). \tag{A 3}$$

But, α is real when $|\omega| < f$ or $|\omega| > N$ and should with the choice (A 3) be positive real so that the terms proportional to $e^{-\alpha z'}$ represent evanescent waves. The combination of negative imaginary α for $if < \omega < iN$ and positive imaginary α for $-iN < \omega < -if$ plus positive real α outside these ranges is obtained when for both $(\omega^2+N^2)^{1/2}$ and $(\omega^2+f^2)^{1/2}$ branch cuts and phases as shown in figure 20 are used. These are just three examples of many possibilities. For each choice of cuts both take the same values when ω lies on the imaginary axis, approaching it from the right.

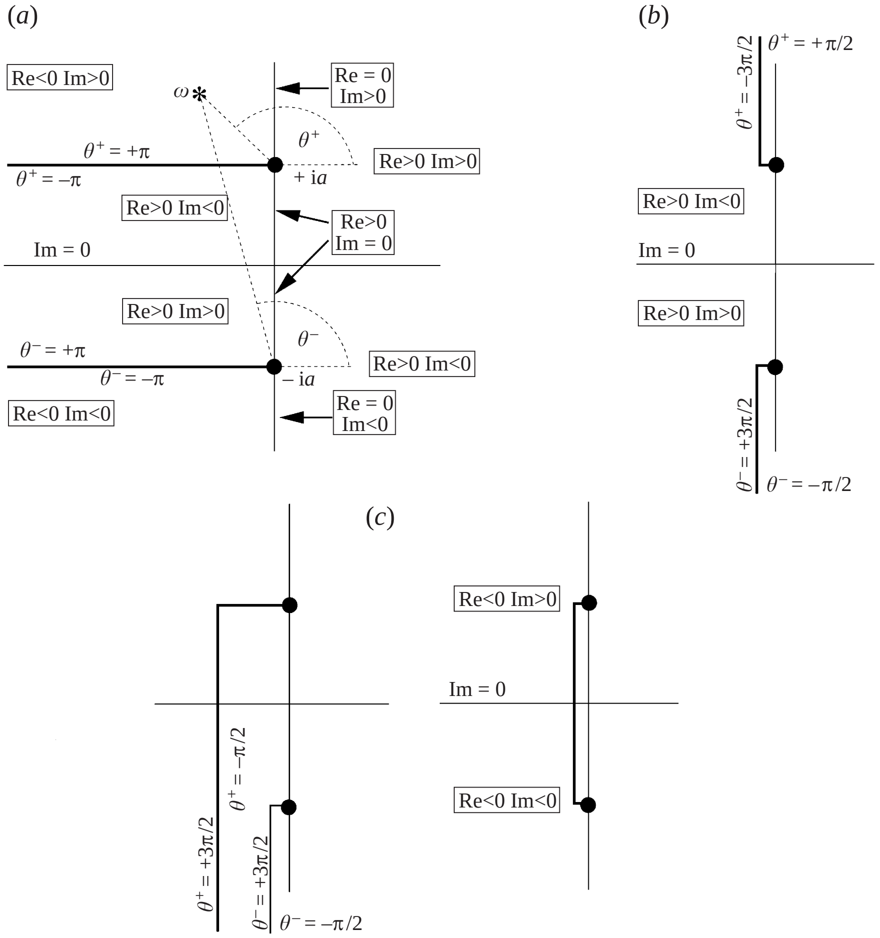

FIGURE 20. A variety of branch cuts for the multi-valued function $(\omega^2+a^2)^{1/2}$. Phases of $\omega-\mathrm{i}a$ and $\omega-(-\mathrm{i}a)$ are θ^+ and θ^-, respectively. Phases and cuts are such that the function has the *same* value when ω lies on the imaginary axis. These are the first Riemann sheets for each case. On crossing a cut the sign of the complex value of the function changes. The lower diagram (*c*) shows how the branch cut running from $-\mathrm{i}a$ to $+\mathrm{i}a$ is a limiting form of where both branch cuts are running downwards and merge below $\omega = -\mathrm{i}a$. Signs of the real and imaginary part have been added to clarify that when for example in (*b*) one enters the second Riemann sheet by crossing the upper branch cut from the right to the left, the function takes the values found in (*a*) above the horizontal branch cut at $\omega = \mathrm{i}a$. Similarly, when in (*c*) the cut is crossed from right to left, then on the second Riemann sheet the function takes the same values as in (*a*) on the first Riemann sheet between the two horizontal branch cuts.

The cuts need not be the same for $(\omega^2+N^2)^{1/2}$ and $(\omega^2+f^2)^{1/2}$. Inspection of (A 1) shows that α behaves as described above. When (A 3) is used, the radiation condition is satisfied and evanescence outside the natural frequency range occurs. For $f > N$ (special case $N = 0$ included) when using (A 3) the radiation condition is also satisfied and evanescence outside the natural frequency range occurs for any combination of branch cuts shown in figure 20. Applying $\mathscr{L}_z^{-1}$ also to the other expressions in (11), using (A 3), we get

$$u(k,l,z;\omega) = (-fil-\omega ik)\frac{(\omega^2+N^2)\mathrm{e}^{-\alpha z'}}{\alpha\omega(\omega^2+f^2)}w_s(k,l;\omega), \qquad \text{(A 4)}$$

$$v(k,l,z;\omega) = (f\mathrm{i}k - \omega\mathrm{i}l)\frac{(\omega^2+N^2)\mathrm{e}^{-\alpha z'}}{\alpha\omega(\omega^2+f^2)}w_s(k,l;\omega), \tag{A 5}$$

$$w(k,l,z;\omega) = -\partial_{z'}\frac{\mathrm{e}^{-\alpha z'}}{\alpha}w_s(k,l;\omega), \tag{A 6}$$

$$p(k,l,z;\omega) = \frac{-(\omega^2+N^2)\mathrm{e}^{-\alpha z'}}{\alpha\omega}w_s(k,l;\omega). \tag{A 7}$$

With the convolution theorem for Fourier and Laplace transforms (Morse & Feshbach 1953) it follows that

$$u(x,y,z;t) = G_u \circ w_s = \int_0^t \iint G_u(x-x', y-y', z; t-t')w_s(x',y';t')\,\mathrm{d}x'\,\mathrm{d}y'\,\mathrm{d}t', \tag{A 8}$$

where G_u is obtained by applying FT^{-1} and $\mathscr{L}_t^{-1}$ to (A 4) with $w_s(k,l;\omega) = 1$. The functions G_v, G_w and G_p are determined in the same way. For FT^{-1} we have to calculate the integral

$$\mathscr{I}(x,y,z;\omega) = \frac{1}{(2\pi)^2}\int_{-\infty}^{+\infty}\int_{-\infty}^{+\infty}\frac{\mathrm{e}^{-\beta(k^2+l^2)^{1/2}z'-\mathrm{i}kx-\mathrm{i}ly}}{(k^2+l^2)^{1/2}}\,\mathrm{d}k\,\mathrm{d}l, \quad \beta = \frac{(\omega^2+N^2)^{1/2}}{(\omega^2+f^2)^{1/2}}, \tag{A 9}$$

where the term $(k^2+l^2)^{-1/2}$ comes from the common factor $1/\alpha$ occurring in (A 4)–(A 7) after setting $\alpha = \beta(k^2+l^2)^{1/2}$. Using the operational relations $\mathrm{FT}^{-1}\{-\mathrm{i}k, -\mathrm{i}l\} = \{\partial_x, \partial_y\}$ we get

$$\left.\begin{aligned} G_u &= (f\partial_y + \omega\partial_x)\frac{(\omega^2+N^2)^{1/2}}{\omega(\omega^2+f^2)^{1/2}}\mathscr{I}, & G_v &= (-f\partial_x + \omega\partial_y)\frac{(\omega^2+N^2)^{1/2}}{\omega(\omega^2+f^2)^{1/2}}\mathscr{I}, \\ G_w &= -\partial_{z'}\frac{(\omega^2+f^2)^{1/2}}{(\omega^2+N^2)^{1/2}}\mathscr{I}, & G_p &= \frac{-(\omega^2+N^2)^{1/2}(\omega^2+f^2)^{1/2}}{\omega}\mathscr{I}, \end{aligned}\right\} \tag{A 10}$$

where the G are functions of $\{x,y,z,\omega\}$. For $z' > 0$ and ω-values such that α has a positive real part (and thus β), the integral (A 9) converges. The answer is

$$\mathscr{I} = \frac{1}{2\pi(\beta^2 z'^2 + r^2)^{1/2}} = \frac{(\omega^2+f^2)^{1/2}}{2\pi R(\omega^2+\omega_i^2)^{1/2}}, \tag{A 11}$$

with R and ω_i given by (15). By the principle of analytic continuation (A 11) is true for the entire ω-plane when the appropriate branch-cuts are made, originating at the points $\omega = \pm\mathrm{i}\omega_i$. For the case $f < N$ and imaginary ω in the ranges $0 < |\omega| < f$ and $N < |\omega| < \infty$ (the evanescent wave regime), β is real and positive with the choice of branch cuts for $(\omega^2+f^2)^{1/2}$ and $(\omega^2+N^2)^{1/2}$ discussed above. In these ω-ranges $\mathscr{I}$ must therefore be positive real. Since $(\omega^2+f^2)^{1/2}$ is positive imaginary when $\omega > \mathrm{i}N$ and because $f^2 \leqslant \omega_i^2 \leqslant N^2$, it follows that for these ω-values $(\omega^2+\omega_i^2)^{1/2}$ has to be positive imaginary. Similarly, $(\omega^2+\omega_i^2)^{1/2}$ has to be negative imaginary when $\omega < -\mathrm{i}N$. Furthermore, $(\omega^2+\omega_i^2)^{1/2}$ should be positive real for $-\mathrm{i}f < \omega < \mathrm{i}f$. These demands are met when the branch cuts and phases for $(\omega^2+\omega_i^2)^{1/2}$ are any of those shown in figure 20. This is also true when $f > N$. Putting (A 11) in (A 10) and using

$\mathscr{L}_t^{-1}\{\omega^n\} = \partial_t^n$ we get (13) with

$$\psi = \mathscr{L}_t^{-1}\{\mathscr{A}\}, \quad h = \mathscr{L}_t^{-1}\{\mathscr{B}\}, \quad \mathscr{A} = \frac{(\omega^2 + N^2)^{1/2}}{2\pi R\omega(\omega^2 + \omega_i^2)^{1/2}},$$

$$\mathscr{B} = \frac{1}{2\pi R(\omega^2 + N^2)^{1/2}(\omega^2 + \omega_i^2)^{1/2}}. \tag{A 12}$$

The contour for $\mathscr{L}_t^{-1}$ runs vertically to the right of the branch points at $\omega = \pm \mathrm{i}N$, $\omega = \pm \mathrm{i}\omega_i$ and the pole at $\omega = 0$ that occurs in $\mathscr{A}$. Alternative contours due to a deformation of the original contour into the left-hand side of the ω-plane are shown below in figure 21. Since $\mathscr{L}_t^{-1}\{(\omega^2 + a^2)^{-1/2}\} = J_0(at)$, $\mathscr{L}_t^{-1}\{(\omega^2 + a^2)^{1/2} - \omega\} = (a/t)J_1(at)$, and $\mathscr{L}_t^{-1}\{\omega^{-1}\} = U(t)$, (14) follows from the convolution theorem.

A.2. *Early-time behaviour*

The result (17) follows directly from inspection of $\mathscr{A}$ and $\mathscr{B}$ in (A 12) with $\omega_i = f = N$ substituted and application of $\mathscr{L}_t^{-1}$. To derive (24) and (25) it is convenient to introduce the forcing at the spectral level. The Fourier spectrum of S is

$$\mathscr{S}(k, l; \varepsilon) = \iint \frac{\varepsilon \mathrm{e}^{\mathrm{i}(kx + ly)}}{2\pi(\varepsilon^2 + x^2 + y^2)^{3/2}} \,\mathrm{d}x\,\mathrm{d}y = \mathrm{e}^{-\varepsilon\sqrt{k^2 + l^2}}. \tag{A 13}$$

Next we substitute $w_s(k, l; \omega) = \mathscr{S}(k, l; \varepsilon)$ in (A 4)–(A 7) and perform FT^{-1} and $\mathscr{L}_t^{-1}$. For FT^{-1} we need to replace $\mathscr{I}$ in (A 10) by $\mathscr{I}_\varepsilon$:

$$\mathscr{I}_\varepsilon(x, y, z; \omega) = \frac{1}{(2\pi)^2} \iint \frac{\mathrm{e}^{-\beta(k^2 + l^2)^{1/2} z' - \varepsilon\sqrt{k^2 + l^2} - \mathrm{i}kx - \mathrm{i}ly}}{(k^2 + l^2)^{1/2}} \,\mathrm{d}k\,\mathrm{d}l$$

$$= \frac{1}{2\pi(r^2 + (\beta z' + \varepsilon)^2)^{1/2}}, \tag{A 14}$$

and calculate $\mathscr{L}_t^{-1}$. For $N = f$ we have $\beta = 1$ (see (A 9)) and the solution is (19) with R replaced by R_ε defined in (24). The quickest way to derive (28) is to substitute power series expansions in t for the Bessel functions in (14). In order to get the results stated in § 3.4 for the finite-sized forcing $w_s = S(r; \varepsilon)\delta(t)$, $\mathscr{I}$ in (A 10) has to be replaced by $\mathscr{I}_\varepsilon$. When $N \neq f$

$$\mathscr{I}_\varepsilon = \frac{(\omega^2 + f^2)^{1/2}}{2\pi R' D(\omega)^{1/2}}, \tag{A 15}$$

where

$$D(\omega) = \omega^2 + \omega_i'^2 - (2\varepsilon z / R'^2)(\omega^2 + f^2)^{1/2}(\omega^2 + N^2)^{1/2}, \tag{A 16}$$

with R' and ω_i' defined in (57). This follows from substitution of β given by (A 9) in (A 14). The response for the various velocity components and pressure are given by (13) with ψ, h as in (A 12) but with $\mathscr{A}, \mathscr{B}$ replaced by

$$\mathscr{A}_\varepsilon = \frac{(\omega^2 + N^2)^{1/2}}{2\pi R' \omega D(\omega)^{1/2}}, \quad \mathscr{B}_\varepsilon = \frac{1}{2\pi R'(\omega^2 + N^2)^{1/2} D(\omega)^{1/2}}. \tag{A 17}$$

By expanding $\mathscr{A}_\varepsilon$ and $\mathscr{B}_\varepsilon$ in inverse powers of ω and using $\mathscr{L}_t^{-1}\{\omega^{-n-1}\} = U(t)t^n/n!$, (24), (25), (32) and (34) are found.

A.3. *Large-time behaviour*

For the point forcing $\psi, h = \mathscr{L}_t^{-1}\{\mathscr{A}\}, \mathscr{L}_t^{-1}\{\mathscr{B}\}$ with $\mathscr{A}, \mathscr{B}$ defined by (A 12). For $w_s = S(r; \varepsilon)\delta(t)$ we have $\psi = \mathscr{L}_t^{-1}\{\mathscr{A}_\varepsilon\}$ and $h = \mathscr{L}_t^{-1}\{\mathscr{B}_\varepsilon\}$ with $\mathscr{A}_\varepsilon, \mathscr{B}_\varepsilon$ defined

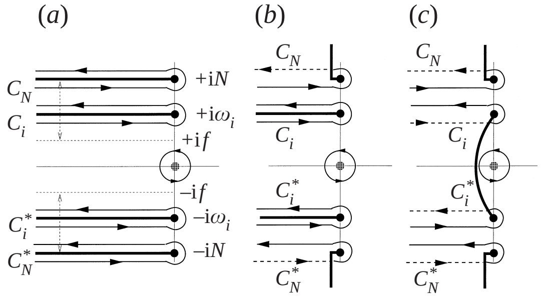

FIGURE 21. Alternative contours for the inverse Laplace transform $\mathscr{L}_t^{-1}$ of $\mathscr{A}$ and $\mathscr{B}$ obtained by deforming the original contour which ran to the right of the branch points and the pole into the left-hand side of the ω-plane. The integrals along the horizontal branch cuts in (*a*) at $\omega = \pm\mathrm{i}N$ give rise to buoyancy oscillations, the integrals along the movable branch cuts at $\omega = \pm\mathrm{i}\omega_i$ determine the internal wave field. The residue of the pole at $\omega = 0$ gives the asymptotic vortex (see text). Different combinations of branch cuts are shown in (*b*) and (*c*). Upon deforming the original inversion contour second Riemann sheets are entered (dashed lines) but the results are the same.

in (A 17) while for the forcing $w_s = S'(r;\varepsilon)\delta(t)$ one has $\psi = \mathscr{L}_t^{-1}\{-\partial_\varepsilon\mathscr{A}_\varepsilon\}$ and $h = \mathscr{L}_t^{-1}\{-\partial_\varepsilon\mathscr{B}_\varepsilon\}$. The following techniques have been used to determine the large-time behaviour of the responses described in § 4.

A.3.1. *Vortices*

For the point forcing (Green's functions) the contour for $\mathscr{L}_t^{-1}$ is deformed into the left half-plane, enclosing the singular points of $\mathscr{A},\mathscr{B}$. There is a pole in $\mathscr{A}$ at $\omega = 0$ when $N \neq 0$. Examples of equivalent contours are shown in figure 21 for $N > f$. The case $N < f$ is entirely analogous. The closed contour about the pole at $\omega = 0$ gives ψ_∞ in (35). This pole is also encountered upon deforming the original contour for $\mathscr{L}_t^{-1}$ when calculating the transform of $\{A_\varepsilon\}$ and $\{-\partial_\varepsilon A_\varepsilon\}$. Examples of equivalent contours are shown below in figure 23. The residues at $\omega = 0$ give (36) and (37), respectively. When in each case $\delta(t)$ is replaced by some $F(t)$ (switch-on forcing) with the Laplace transform $\mathscr{F}(\omega)$ then

$$\lim_{t\to\infty}\int_0^t F(t')\,\mathrm{d}t' \equiv M(\infty) = \lim_{\omega\to 0}\mathscr{F}(\omega).$$

The asymptotic vortex is determined by the behaviour of $\mathscr{F}(\omega)\mathscr{A}(\omega)$ in the vicinity of $\omega = 0$ for $w_s = \delta(x)\delta(y)F(t)$ and for $w_s = S(r;\varepsilon)F(t)$ and $w_s = S'(r;\varepsilon)F(t)$ by $\mathscr{F}(\omega)\mathscr{A}_\varepsilon(\omega)$. If $M(\infty) \neq 0$ then $\mathscr{F}(0) \neq 0$ and the pole from the factor $1/\omega$ in $\mathscr{A},\mathscr{A}_\varepsilon$ remains. The residue changes by a factor $M(\infty)$ and the asymptotic vortices (35), (36) and (37) form again but multiplied by an overall factor $M(\infty)$. When $M(\infty) = 0$ we cannot immediately conclude that the vortices vanish asymptotically. This will only be true if $F(t)$ is such that to leading order $\mathscr{F}(\omega) \propto \omega^{n+1}$ for $\omega \approx 0$, where $n = 0,1,2,\cdots$. The following class of functions has this property. Let $F(t) = \mathrm{d}_t G(t)$ with $G(t)$ some smooth function with the properties $0 < \left|\int_0^\infty G(t')\,\mathrm{d}t'\right| < \infty$ and $G(0) = 0$ and $\lim_{t\to\infty} G(t) = 0$. This implies $\int_0^\infty F(t')\,\mathrm{d}t' = M(\infty) = 0$ and $\mathscr{F}(\omega) = \omega\mathscr{G}(\omega)$ with $\mathscr{G}(\omega) = \mathscr{L}_t\{G(t)\}$. Since we assumed $0 < \left|\int_0^\infty G(t')\,\mathrm{d}t'\right| < \infty$ we have $\mathscr{G}(0) \neq 0$ and $\mathscr{F} \approx \omega\mathscr{G}(0)$ for $\omega \approx 0$ which cancels the pole in $\mathscr{A},\mathscr{A}_\varepsilon$ and asymptotically the vortices vanish. This class of functions has $n = 0$. Cases with $n > 0$ are those where $F(t) = \mathrm{d}_t^{n+1}G(t)$ with $\left|\int_0^\infty G(t')\,\mathrm{d}t'\right| > 0$ and G and its derivatives up to order n vanishing at $t = 0,\infty$ With the above restrictions on $F(t)$ when $M(\infty) = 0$ it follows that the asymptotic vortex's amplitude is proportional to $M(\infty)$.

A.3.2. *Asymptotic waves and buoyancy oscillations for Green's functions*

Both $\mathscr{A}$ and $\mathscr{B}$ have branch points at $\omega = \pm\mathrm{i}\omega_i$ and at $\omega = \pm\mathrm{i}N$. Branch cuts and phases for the multi-valued functions $(\omega^2 + N^2)^{1/2}$, $(\omega^2 + \omega_i^2)^{1/2}$ can be any of those shown in figure 20. Branch-cut integrals result when the contour for $\mathscr{L}_t^{-1}$ is deformed into the left-hand side of the complex ω-plane. Examples are shown in figure 21. The same result is obtained in each example, even when sections of the contours lie on the second Riemann sheet (indicated by dashed lines). This follows from figure 20 where we indicated the values the functions take depending on the choice of cuts. Their choice was dictated by the radiation condition. The *movable* branch cut from $\mathrm{i}\omega_i$ can lie anywhere between the extremes $\mathrm{i}f$ and $\mathrm{i}N$ as indicated by the arrows in the first example in figure 21. Only the integrals along C_i, C_N have to be calculated because along $C^{\star}_{N,i}$ the complex conjugate is obtained. Thus, $\mathscr{L}_t^{-1}\{\mathscr{A},\mathscr{B}\} = (C_i + C_i^{\star}) + (C_N + C_N^{\star}) + \mathrm{Res}_{\omega=0}$, where the residual term occurs for $\mathscr{A}$ when $N \neq 0$. The branch cut integrals give rise to the 'wavy' part of the response. $\mathscr{A}$ and $\mathscr{B}$ are developed for C_N in powers of $s = (\omega - \mathrm{i}N)^{1/2}$ and for C_i in powers of $s = (\omega - \mathrm{i}\omega_i)^{1/2}$, i.e. series of the form $\sum_n \alpha_n s^{n-1/2}$ are used. Integration along for example C_N yields a series $\pi^{-1}\mathrm{e}^{\mathrm{i}Nt}\left[\alpha_0 t^{-1/2} + \sum_{n=1}^{\infty}(-1)^n\Gamma(n+\frac{1}{2})\alpha_n t^{-n-1/2}\right]$ because

$$(2\pi\mathrm{i})^{-1}\int_{-\infty}^{(0)^+} s^{n-1/2}\mathrm{e}^{st}\,\mathrm{d}s = \pi^{-1/2}\,\mathrm{d}_t^n t^{-1/2} = \pi^{-1}(-1)^n\Gamma\left(n+\tfrac{1}{2}\right)t^{-n-1/2}. \qquad \text{(A 18)}$$

$\int_{-\infty}^{(0)^+}\mathrm{d}s$ indicates an integration path coming from $-\infty$ along the real axis in the s-plane which loops around the origin (the branch point) in the positive direction and then returns to $-\infty$ along the real axis. Because of the multi-valuedness of $s^{n-1/2}$ the two parts do not cancel each other. With branch cuts and phases as in figure 20 the result is (A 18). Using this to evaluate the branch-cut integrals one gets (38). Mathematically the required longer waiting period for (38) to be valid to a given degree of precision when $\omega_i \approx N$ is because the branch points at $\omega = \mathrm{i}\omega_i$ and $\omega = \mathrm{i}N$ get close to each other in figure 21. The time when the two contours C_i and C_N give well-separated contributions scales with the inverse of the separation distance between the branch points, i.e. roughly with $|N - \omega_i|^{-1}$. Similar remarks apply to the special case $N = 0$ or $f = 0$ where when $\omega_i \approx 0$ the asymptotic results are only valid for large time $t \gg \omega_i^{-1}$ because the branch points at $\omega = \pm\mathrm{i}\omega_i$ become close.

A.3.3. *Asymptotic waves and oscillations for a finite-sized forcing*

Internal gravity waves are associated with movable branch points which are roots of $D(\omega) = 0$. $D(\omega)$ can be factorized as follows:

$$D(\omega) = \left(\frac{r^2+\varepsilon^2}{R'^2}\right)[(\omega^2+f^2)^{1/2}+\varrho(\omega^2+N^2)^{1/2}][(\omega^2+f^2)^{1/2}+\varrho^{\star}(\omega^2+N^2)^{1/2}], \qquad \text{(A 19)}$$

where

$$\varrho = z/(\mathrm{i}r - \varepsilon), \quad R'^2 = (r^2 + \varepsilon^2 + z^2). \qquad \text{(A 20)}$$

Roots of $D(\omega) = 0$ are

$$\omega_{\pm} = \mp\left(\frac{\varrho^2 N^2 - f^2}{1-\varrho^2}\right)^{1/2}, \quad \omega_{\pm}^{\star} = \pm\left(\frac{\varrho^{\star 2}N^2 - f^2}{1-\varrho^{\star 2}}\right)^{1/2}. \qquad \text{(A 21)}$$

The values have been made unambiguous by taking for the complex terms $(\varrho^{(\star)^2}N^2 - f^2)/(1 - \varrho^{(\star)^2})$ phases φ with $-\pi < \varphi \leqslant \pi$. For $z, r \neq 0$ the roots are symmetrically

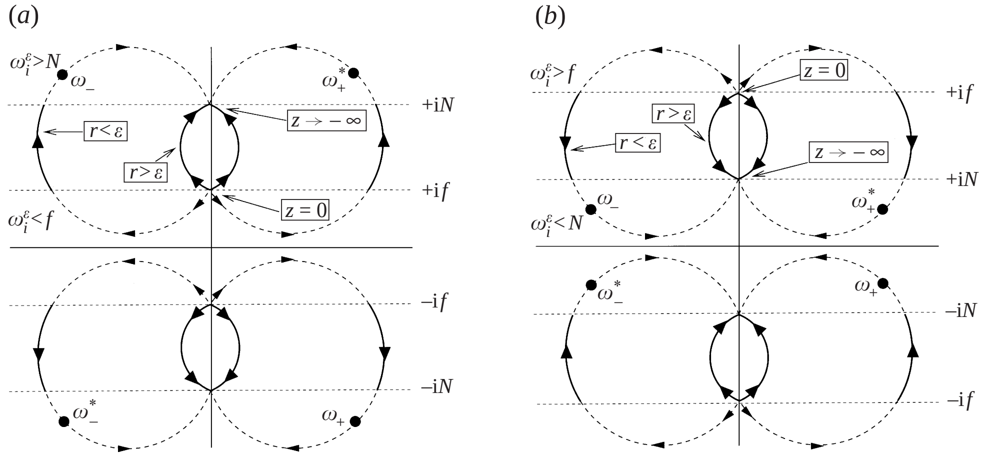

FIGURE 22. Location of the roots of $D(\omega) = 0$ as a function of observer position. For $r > \varepsilon$ the imaginary parts of the roots always lie in the natural frequency range (solid lines), for $r < \varepsilon$ they can lie outside the natural frequency ranges (dashed lines). Examples are for (*a*) $N > f$ and (*b*) $N < f$. Arrows indicate increasing depth $|z|$.

positioned about the real and imaginary axis in the ω-plane

$$\omega_- = -\omega_r + i\omega_i^\varepsilon \quad \omega_-^\star = -\omega_r - i\omega_i^\varepsilon \quad \omega_+ = \omega_r - i\omega_i^\varepsilon \quad \omega_+^\star = \omega_r + i\omega_i^\varepsilon. \qquad (\mathrm{A}\,22)$$

In figure 22 we show schematically how the position of ω_i^ε and ω_r vary with the observer position. For $r > \varepsilon$ the roots have for all z an imaginary part ω_i^ε in the natural frequency range, i.e. in figure 22(*a*) $f \leqslant \omega_i^\varepsilon(r > \varepsilon, z) < N$ while in figure 22(*b*) $N < \omega_i^\varepsilon(r > \varepsilon, z) \leqslant f$. When $r < \varepsilon$ there are ranges of z where ω_i^ε lies outside the natural frequency range.

The approximations for ω_i^ε and ω_r (57) in the far field were derived by expanding $D(\omega)^{-1/2}$ in powers of $\varepsilon z/R'^2$:

$$\frac{1}{D(\omega)^{1/2}} = \frac{1}{(\omega^2 + \omega_i'^2)^{1/2}} \left[1 + \sum_{n=1}^{\infty} \alpha_n b^n \left(\frac{(\omega^2 + f^2)^{1/2}(\omega^2 + N^2)^{1/2}}{(\omega^2 + \omega_i'^2)} \right)^n \right], \qquad (\mathrm{A}\,23)$$

where

$$\alpha_n = \frac{(-1)^n (2n-1)\cdot(2n-3)\cdots 5\cdot 3\cdot 1}{2^n n!}, \quad b = \frac{-2\varepsilon z}{R'^2}, \qquad (\mathrm{A}\,24)$$

and ω_i' given by (57). Thus, in this far-field approximation the branch points associated with the internal gravity waves are located at $\omega = \pm i\omega_i'$. The next step is suspect but leads to a good approximation. We expand (A 23) in powers of $(\omega - i\omega_i')$ and keep for each n in the series only the highest negative power of $(\omega - i\omega_i')$. That is, we approximate (A 23) near $\omega = i\omega_i'$ by

$$\frac{1}{D(\omega)^{1/2}} \approx \frac{1}{(2i\omega_i')^{1/2}(\omega - i\omega_i')^{1/2}} \times \left[1 + \sum_{n=1}^{\infty} \alpha_n b^n \left(\frac{(f^2 - \omega_i'^2)^{1/2}(N^2 - \omega_i'^2)^{1/2}}{2i\omega_i'} \right)^n \frac{1}{(\omega - i\omega_i')^n} \right]. \qquad (\mathrm{A}\,25)$$

To calculate $\psi_i = \mathscr{L}_t^{-1}\{\mathscr{A}_\varepsilon\}$, which determines the horizontal velocity components and pressure, the remaining prefactor in $\mathscr{A}_\varepsilon$ (A 17) is also expanded in powers of

$(\omega - \mathrm{i}\omega_i')$ and approximated by retaining only the lowest-order term

$$\frac{(\omega^2 + N^2)^{1/2}}{2\pi R'\omega} \approx \frac{(N^2 - \omega_i'^2)^{1/2}}{2\pi R'\mathrm{i}\omega_i'}. \tag{A 26}$$

We multiply (A 25) by (A 26) and perform the branch-cut integral. Using

$$\mathscr{L}_t^{-1}\{(\omega - \mathrm{i}\omega_i')^{-1/2-n}\} = \frac{2^n t^{n-1/2} \mathrm{e}^{\mathrm{i}\omega_i' t}}{\sqrt{\pi}(2n-1)\cdot(2n-3)\cdots 5\cdot 3\cdot 1} \quad (n = 1, 2, \ldots) \tag{A 27}$$

we get after adding the complex conjugate

$$\psi_i \approx 2\mathrm{Re}\,\frac{(N^2 - \omega_i'^2)^{1/2}\mathrm{e}^{\mathrm{i}(\omega_i' t - 3\pi/4)}}{(2\pi)^{3/2} R' \omega_i'^{3/2} t^{1/2}} \left[1 + \sum_{n=1}^{\infty} \frac{(-b)^n}{n!} \left(\frac{(f^2 - \omega_i'^2)^{1/2}(N^2 - \omega_i'^2)^{1/2}}{2\mathrm{i}\omega_i'}\right)^n t^n\right]. \tag{A 28}$$

For (A 27) a phase and cut as shown in figure 20 for $(\omega - \mathrm{i}\omega_i)^{1/2}$ is used. This is the correct choice because if we let $\varepsilon \to 0$ in (A 28) we get the leading-order behaviour of ψ_i for the Green's function given by (38). Had we not approximated (A 23) by (A 25) and used (A 26), then for each n in this series there would have been additional terms of order $t^{n-1}, t^{n-2}, \ldots$. We have retained with the approximations the 'worst' possible divergent sub-sequence. The term in square brackets in (A 28) is recognized as the expansion of an exponential. Substituting b from (A 24) we get

$$[\cdots] = \exp\left(\frac{\varepsilon z |(f^2 - \omega_i'^2)^{1/2}(N^2 - \omega_i'^2)^{1/2}|}{\omega_i' R'^2} t\right), \tag{A 29}$$

where we used the properties of $(\omega^2 + f^2)^{1/2}$ and $(\omega^2 + N^2)^{1/2}$ on the first Riemann sheets defined in figure 20, which were chosen to satisfy the radiation condition. For $z < 0$ (underneath the surface) (A 29) is an amplitude that decays exponentially with time. In this fashion (57) was derived. It implies that in the inverse Laplace transform for the far field we pick up contributions from approximations of ω_- and $\omega_-^\star$, i.e. the zeros of $D(\omega)$ in the left-half of the ω-plane. Since the inversion contour has to be to the right of all the singularities of the integrand, it appears that there are no contributions from ω_+ and $\omega_+^\star$. Further analysis of (A 19) shows that ω_- and $\omega_-^\star$ are indeed the only zeros of $D(\omega)$ when the first sheets of $(\omega^2 + f^2)^{1/2}$ and $(\omega^2 + N^2)^{1/2}$ are used while ω_+ and $\omega_+^\star$ are roots of $D(\omega) = 0$ if the second sheet of either $(\omega^2 + f^2)^{1/2}$ or $(\omega^2 + N^2)^{1/2}$ is used. The branch points at ω_+ and $\omega_+^\star$ are therefore 'invisible' to the inversion contour.

In figure 23 we sketch what happens when the contour for the inversion is deformed into the left-hand side of the ω-plane. Branch points are found at $\omega = \omega_-^{(\star)}$ and cuts need to be made. A simple example is shown in figure 23(*a*) where all branch cuts are parallel to each other. When $|\mathrm{Im}\,\omega_-^{(\star)}| = \omega_i^\varepsilon$ is in the natural frequency range, the contour wraps around these branch cuts, indicated by $C_-^{(\star)}$ (Im denotes the imaginary part of a complex quantity). Also integrals along the cuts for $(\omega^2 + f^2)^{1/2}$ and $(\omega^2 + N^2)^{1/2}$ result, indicated by $C_f^{(\star)}$ and $C_N^{(\star)}$, respectively. On the right-hand side the branch points at $\omega = \omega_+^{(\star)}$ are shown, with open circles to indicate that they do not lie on the Riemann sheet where the inversion takes place. A pole at $\omega = 0$ is encountered for $\psi = \mathscr{L}_t^{-1}\{\mathscr{A}_\varepsilon\}$ when $N \neq 0$, which results in the asymptotic vortex (36). As the observer position varies $\omega_-^{(\star)}$ can cross one of the fixed cuts as indicated by the arrows. This is when we enter the 'unnatural' regions shown in figures 13 and 14.

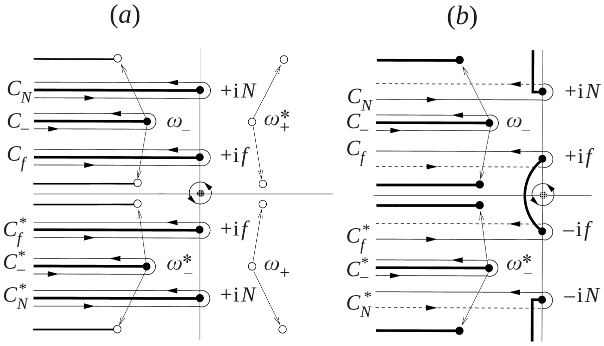

FIGURE 23. Alternative contours for the inverse Laplace transform $\mathscr{L}_t^{-1}$ of $\mathscr{A}_\varepsilon$ and $\mathscr{B}_\varepsilon$ resulting from a deformation of the original contour into the left-hand side of the ω-plane. Phases and cuts for the multi-valued functions defining the first Riemann sheets of $(\omega^2+f^2)^{1/2}$ and $(\omega^2+N^2)^{1/2}$ are as in figure 20. The branch points ω_+ and $\omega_+^\star$ (open circles) always lie on a Riemann sheet entered by crossing one of the branch cuts of $(\omega^2+f^2)^{1/2}$ or $(\omega^2+N^2)^{1/2}$. They are not encountered when the contour is deformed. In (*a*) the branch points ω_- and $\omega_-^\star$ only lie on the Riemann sheet of the inversion when ω_i^ε is in the natural frequency range (closed circles) but cross a cut when ω_i^ε is outside the natural frequency range (open circles). This occurs only when $r<\varepsilon$ (see figure 13). In (*b*) ω_- and $\omega_-^\star$ always lie on the Riemann sheet of the inversion but are not encountered if ω_i^ε is outside the natural range when the contour is deformed across the branch cuts of $(\omega^2+f^2)^{1/2}$ and $(\omega^2+N^2)^{1/2}$ (dashed sections). The pole at $\omega=0$ results in the asymptotic vortices (36) and (37).

An open symbol is assigned to $\omega_-^{(\star)}$ in that case to indicate that they no longer lie on the first sheet. Now the deformed contour does not encounter the singularities at $\omega_-^{(\star)}$. In figure 23(*b*) we give an example of a more complex combination of branch cuts for $(\omega^2+f^2)^{1/2}$ and $(\omega^2+N^2)^{1/2}$ that could be used to satisfy the radiation condition. Again the singularities at $\omega=\omega_+^{(\star)}$ (not shown) do not lie on the Riemann sheet under consideration. The contour can be deformed across the cuts for $(\omega^2+f^2)^{1/2}$ and $(\omega^2+N^2)^{1/2}$ (dashed lines indicate when the contour lies on the second sheet of the function). But, the results are the same for $C_N^{(\star)}$ and $C_f^{(\star)}$ in figure 23(*a*) and 23(*b*). When ω_i^ε is in the natural frequency range, the same contour integrals $C_-^{(\star)}$ as in figure 23(*a*) occur. However, $\omega_-^{(\star)}$ stays on the first Riemann sheet when ω_i^ε moves outside the natural frequency range. Again the branch points are not encountered when the contour is deformed across the cuts for $(\omega^2+f^2)^{1/2}$ and $(\omega^2+N^2)^{1/2}$.

For the branch cut integral C_-, $D(\omega)$ is developed in powers of $(\omega-\omega_-)$. By writing $D(\omega)$ as

$$D(\omega)=\left(\frac{r^2+\varepsilon^2}{R'^2}\right)\frac{(1-\varrho^2)(1-\varrho^{\star 2})(\omega-\omega_-)(\omega-\omega_-^\star)(\omega-\omega_+)(\omega-\omega_+^\star)}{[(\omega^2+f^2)^{1/2}-\varrho(\omega^2+N^2)^{1/2}][(\omega^2+f^2)^{1/2}-\varrho^\star(\omega^2+N^2)^{1/2}]},\tag{A 30}$$

it follows that the first term in this expansion is $(\omega-\omega_-)2\mathrm{i}\omega_i^\varepsilon P$ where

$$P=\left(\frac{r^2+\varepsilon^2}{R'^2}\right)\frac{(1-\varrho^2)(1-\varrho^{\star 2})(\omega_--\omega_+)(\omega_--\omega_+^\star)}{[(\omega_-^2+f^2)^{1/2}-\varrho(\omega_-^2+N^2)^{1/2}][(\omega_-^2+f^2)^{1/2}-\varrho^\star(\omega_-^2+N^2)^{1/2}]}.\tag{A 31}$$

To leading order (58), (59) and (60) result when the complex conjugate is added. The integrals along C_N and $C_N^\star$ give (76). The longer time required for (76) to be valid when $N \approx \omega_i'$ is that then either the upper or lower leg of the contour C_N comes close to the branch point at $\omega = \omega_-$ (see figure 23). The contour integral along C_f and its conjugate, leading to (78) and (79), is also straightforward. The longer time required for (78) and (79) to be valid when $f \approx \omega_i'$ is that then the contour C_f runs close to the branch-point at $\omega = \omega_-$ (see figure 23).

REFERENCES

Batchelor, G. K. 1967 *An Introduction to Fluid Dynamics*. Cambridge University Press.

Bleistein, N. & Handelsman, R. A. 1986 *Asymptotic Expansions of Integrals*. Dover.

Bretherton, F. P. 1967 The time-dependent motion due to a cylinder moving in an unbounded rotating or stratified fluid. *J. Fluid Mech.* **28**, 545–570.

Charney, J. G. 1955 The generation of ocean currents by wind. *J. Mar. Res.* **14**, 477–498.

Dickinson, R. E. 1969 Propagators of atmospheric motion. 1. Excitation by point impulses. *Rev. Geophys.* **7**, 483–514.

Eckart, C. 1960 *Hydrodynamics of Oceans and Atmospheres*. Pergamon.

Felsen, B. L. & Marcuvitz, N. 1972 *Radiation and Scattering of Waves*. Prentice Hall.

Gill, A. E. 1982 *Atmosphere-Ocean Dynamics*. Academic.

Gordeichik, B. N. & Ter-Krikorov, A. M. 1996 Uniform approximations of the fundamental solution of the equation of internal waves. *J. Appl. Math. Mech.* **60**, 439–447.

Hart, R. W. 1981 Generalized scalar potentials for linearized three-dimensional flows with vorticity. *Phys. Fluids* **24**, 1418–1420.

Hendershott, M. C. 1969 Impulsively started oscillations in a rotating stratified fluid. *J. Fluid Mech.* **36**, 513–527.

Lighthill, M. J. 1978 *Waves in Fluids*. Cambridge University Press.

Morgan, G. W. 1953 Remarks on the problem of slow motions in a rotating fluid. *Proc. Camb. Phil. Soc.* **49**, 362–364.

Morse, P. M. & Feshbach, H. 1953 *Methods of Theoretical Physics. Part 1*. McGraw-Hill.

Olbers, D. J. 1983 Models of the Oceanic internal wave field. *Rev. Geophys. Space Phys.* **21**, 1567–1606.

Pedlosky, J. 1979 *Geophysical Fluid Dynamics*. Springer.

Phillips, O. M. 1963 Energy transfer in rotating fluids by reflexion of inertial waves. *Phys. Fluids* **6**, 513–520.

Voisin, B. 1991 Internal wave generation in uniformly stratified fluids. Part 1. Green's functions and point sources. *J. Fluid Mech.* **231**, 439–480.